Assessment of alternative adsorption models and global sensitivity analysis to characterize Hexavalent chromium loss from soil to surface runoff

Chuan-An Xia[1, 2], Juxiu Tong[1, 2*], Bill X. Hu[1, 2, 3], Xiujie Wu[1, 2], Alberto Guadagnini[4, 5]

Accepted in *Hydrological Processes*

1. School of Water Resources and Environment, China University of Geosciences, Beijing, China 100083

2. Key Laboratory of Groundwater Cycle and Environment Evolution (China University of Geosciences), Ministry of Education, Beijing, China 100083

3. Institute of Groundwater and Earth Sciences, Jinan University, Guangzhou, China 510632

4. Dipartimento di Ingegneria Civile e Ambientale, Politecnico di Milano, Milano, Italy

5. Department of Hydrology and Atmospheric Sciences, The University of Arizona, Tucson, USA

*****Corresponding author: Juxiu Tong

Tel:

E-mail address: juxiu.tong@cugb.edu.cn

Abstract

We investigate our ability to assess transfer of hexavalent chromium, Cr(VI), from the soil to surface runoff by considering the effect of coupling diverse adsorption models with a two-layer solute transfer model. Our analyses are grounded on a set of two experiments associated with soils characterized by diverse particle size distributions. Our study is motivated by the observation that Cr(VI) is receiving much attention for the assessment of environmental risks due to its high solubility, mobility, and toxicological significance. Adsorption of Cr(VI) is considered to be at equilibrium in the mixing layer under our experimental conditions. Four adsorption models, i.e., the Langmuir, Freundlich, Temkin, and the linear model, constitute our set of alternative (competing) mathematical formulations. Experimental results reveal that the soil samples characterized by the finest grain sizes is associated with the highest release of Cr(VI) to runoff. We compare the relative abilities of the four models to interpret experimental results through Maximum Likelihood model calibration and four model identification criteria (i.e., the information criteria AIC and AIC_C, and the Bayesian criteria BIC and KIC). Our study results enable us to rank the tested models on the basis of a set of posterior weights assigned to each of them. A classical variance-based global sensitivity analysis is then performed to assess the relative importance of the uncertain parameters associated with each of the models considered, within sub-regions of the parameter space. In this context, the modeling strategy resulting from coupling the Langmuir isotherm with a two-layer solute transfer model is then evaluated as the most skillful for the overall interpretation of both sets of experiments. Our results document

that (*a*) the depth of the mixing layer is the most influential factor for all models tested, with the exception of the Freundlich isotherm, and (*b*) that the total sensitivity of the adsorption parameters varies in time, with a trend to increase as time progresses for all of the models. These results suggest that adsorption has a significant effect on the uncertainty associated with the release of Cr(VI) from the soil to the surface runoff component.

Keywords: Cr(VI) loss; surface runoff; model ranking; global sensitivity analysis

INTRODUCTION

According to the soil assessment results of China nationwide Multi-Purpose Regional Geochemical Survey (MPRGS) project, considerable portions of lands used for agriculture purpose in China show pollution signatures by metals. Chemical transfer from the soil to surface runoff is a key process that contributes to non-point source pollution. Metals (e.g., Cd, Pb and Cr) originating from a contaminated soil can then contaminate surface water and groundwater, with a negative impact on human health and various compartments of the ecosystem (Krishna and Govil, 2008). Among these pollutants, Cr(VI) has received much attention because of its high solubility, mobility, and toxicological significance in the environment.

Numerous studies focus on efficient methods (*a*) to reduce the amounts of Cr(VI) in the environment, (*b*) to investigate the fate of Cr(VI) in soil and groundwater, and (*c*) to monitor space-time distributions of Cr(VI) in surface runoff. He et al. (2004) monitored metal (i.e., Cd, Co, Cr, Cu, Fe, Ni, Pb, Zn, Mn, and Mo) concentrations in surface runoff at 11 sites in Florida and documented a positive correlation between concentrations of the analyzed metals in runoff and soil. Ghosh et al. (2012) found that Cr(VI) could be successfully adsorbed onto the fine-grained soil used as a liner material in a landfill. Núñez-Delgado et al. (2015) found that both pine sawdust and oak wood ash could be used (as biosorbents) to reduce the concentration of Cr(VI) released from soil to water.

Migration of Cr(VI) through a soil system is typically described by advection, dispersion, adsorption and reaction processes. Advection is controlled by the mean flow rate of water, and dispersion is characterized by molecular diffusion and mechanical

dispersion. Langmuir (1918), Freundlich (1907), and linear isotherm models are often used to simulate Cr(VI) adsorption experimental results under equilibrium assumption (e.g., Ghosh et al., 2012; Núñez-Delgado et al., 2015; Sangiumsak and Punrattanasin, 2014; Mendonca et al., 2013; Fifi et al., 2013; Li et al., 2014). Gupta and Bahu (2009) successfully simulated breakthrough curves of Cr(VI) by combining the Langmuir model with a mathematical transport model. Chakraborty et al. (2015) embedded the Langmuir and linear isotherms, respectively, in a one-dimensional advection-dispersion-reaction-equation to estimate Cr(VI) transport parameters. Such isotherms have also been integrated in well-known numerical codes (e.g., Hydrus-1D (Šimůnek et al., 2009) and MT3DMS (Zheng et al., 1998)) to simulate reactive solute migration. Transport of Cr(VI) is affected by the redox reaction of Cr, associated with Cr(III) and/or Cr(VI) in the environment. Based on thermodynamics, Cr(III) oxidation should be a spontaneous process. However, it needs to be catalyzed to take place in a natural system, due to its very slow kinetics (Apte et al., 2005). In this context, one can note that while chromium is highly mobile with flow in the hexavalent form, its migration would be strongly retarded in the trivalent form because of the typically strong adsorption capacity of soil to Cr(III). It is therefore worth noting that detectable amounts of chromium found in natural waters are usually in the hazardous hexavalent form, manganese oxides essentially being the materials that can oxidize Cr(III) to Cr(VI) in a natural system (Fendorf and Zasoski, 1992). Organic materials, such as sulfides, and ferrous iron, can reduce Cr(VI) to Cr(III) (Fendorf, 1995). We refer to Fendorf (1995) for a comprehensive review on this aspect.

Transfer of a chemical from soil to surface runoff is a complex process. Most of the experimental studies on this process are conducted at the laboratory scale (sand boxes). Various chemical transport models have been developed to explain experimental results. Modeling methods based on the diffusion (Wallach and van Genuchten, 1990) and the mixing-layer theory (Donigian et al., 1977) were the two approaches generally used to simulate the process. The diffusion theory assumes that chemical exchange between runoff and soil is controlled by an accelerated diffusion process. The theory has been used in a variety of studies (Ahuja et al., 1981, 1983; Sharpley et al., 1980), even though the function to describe the accelerated diffusion process is somewhat arbitrarily chosen (Gao et al., 2004). Note that using an accelerated diffusion coefficient in the simulations may aptly capture a set of experimental data, while providing no explanation to the physical mechanism of the diffusion process. Because the physical mechanism in the accelerated diffusion theory remains unclear, the diffusion theory has limited ability for prediction.

The mixing-layer theory was first proposed by Donigian et al. (1977). It is based on the assumption that surface runoff water mixes entirely and instantaneously with soil water in a thin layer on the soil surface with no contribution from the soil below such a mixing layer. However, Zhang et al. (1997) found that the diffusion flux from the soil underlying the mixing layer could not be neglected under poor drainage conditions. Therefore, Zhang et al. (1999) used the convection-diffusion equation to simulate the diffusion flux from the underlying soil.

A series of mechanistic models have been developed in recent years. Soil erosion

127 was characterized by the Rose model (Rose et al., 1994; Hairsine and Rose, 1991), and
128 solute transfer between the runoff and the exchange layers was determined by the water
129 transfer rate. Gao et al. (2004) assumed that the solute transfer from soil to surface
130 runoff was affected by both drop-liquid and drop-liquid-solid interactions, and the
131 process was conceptualized as the model of the three layers/compartments, i.e., a runoff,
132 an exchange, and the underlying soil compartment. Tong et al. (2010) proposed a new
133 model to integrate the runoff and the mixing layers into a unique mixing region. In the
134 model, solute concentration in the runoff was calculated as αC_w, where α $(0 < \alpha \le 1)$
135 is an incomplete mixing coefficient and C_w is the aqueous-phase solute concentration
136 in the mixing layer [M L^{-3}]. The net chemical flux from the mixing layer to the
137 underlying soil is calculated as $i\gamma C_w$, and i and γ $(0 < \gamma \le 1)$ are, respectively, the
138 infiltration rate [L T^{-1}] and another incomplete mixing coefficient. All of these models
139 assume that the soil surface is (nearly) horizontal, the thickness of the mixing layer is
140 regarded as stable or constant, and lateral and return flows in the soil are negligible.
141 Dong and Wang (2013) considered an inclined soil surface and relied on the conceptual
142 model of Gao et al. (2004). They assumed solute concentrations in the runoff and the
143 mixing layer were to be identically affected by raindrop splash. In addition, the model
144 allows the mixing layer to have a variable depth, and takes into account the effects of
145 raindrop splash, lateral flow, and return flow. Notably, solute concentrations in the
146 mixing and/or exchange layers are considered as uniform.

147 The main considered factors affecting Cr(VI) transfer from soil to surface runoff in
148 the above referenced models include rain intensity (Gao et al., 2004), ponding water

depth (Gao et al., 2004), soil characteristics (Tong et al., 2010), soil slope (Dong and Wang 2013), and drainage conditions (Walker et al., 2007; Zhang et al., 1999). Adsorption of a chemically active solute is another important factor that affects solute loss. Gao et al. (2004) integrated the linear adsorption model with a solute loss model to evaluate phosphorus concentrations in runoff. In this broad context, it is still lack of a detailed study on the influence of the adsorption model choice on Cr(VI) loss simulation from soil to surface runoff.

An objective of our study is to evaluate the impact of a model selected from a set of differing adsorption models (i.e., the Langmuir, Freundlich, Temkin and linear models) on the Cr(VI) loss simulation. We do so by relying on a set of two experiments and grounding our study on rigorous model identification criteria (Neuman, 2003; Ye et al., 2004, 2008; Neuman et al., 2012; Bianchi-Janetti et al., 2012). These enable us to (*a*) compare the ability of each of the tested models to interpret the target experimental results and (*b*) rank the models through the evaluation of probabilistic weights assigned to each of them. We then provide model-averaged estimates (and associated uncertainty bounds) of Cr(VI) concentrations in runoff by leveraging on the diverse interpretive skills of all models analyzed. Since each of the models is associated with a set of typically unknown/uncertain parameters, we also perform a classical variance-based global sensitivity analysis to assess the relative contribution of the uncertain parameters associated with each model to the variability of Cr(VI) released from the soil to surface runoff.

The rest of the study is structured as follows. We first provide descriptions for the

171 experiments performed and for the modeling approaches. We then present and discuss
172 our results, in terms of model ranking and multi-model analysis as well as global
173 sensitivity analysis. We finally make our conclusions.
174
175 ## MATERIALS AND METHODS
176 *Soil Chemical characteristics*
177 Representative silt soil samples obtained from the region surrounding the city of
178 Wuhan, China, were dried, ground and passed through 2 mm and 1 mm sieves, to form
179 the two subsamples, respectively termed soil sample 1 and 2, employed in our
180 experimental investigations. Table 1 lists the main chemical characteristics of soil 2.
181 The latter is seen to be characterized by a very low initial Cr(VI) concentration, the
182 overall picture suggesting that the soil is oxic. As such, we do not consider Cr(VI)
183 reduction in our experimental investigations.
184 *Experiments*
185 We leverage on the experimental set-up used by Tong et al. (2010), to which we refer
186 for additional details. In summary, a steel sandbox (with length, width and depth
187 respectively of 100, 30, and 40 cm) with rustproof paint and equipped with two drainage
188 holes at the bottom was used (see Fig. 1). A 5-cm-thick layer of gravel is packed at the
189 bottom of the sand box to allow for water drainage. The elevations of the drainage
190 outlets can be modified to achieve diverse drainage conditions. The gravel layer is
191 covered with a nylon screen to prevent loss of soil particles, the soil subject to the
192 experiments being packed above the screen. A rectangular hatch that opens into a V-
193 shaped trench and located 30 cm above the bottom of the box is used to collect surface

runoff water. The height difference between the soil surface and the runoff hatch corresponds to the depth of ponded water. A rainfall simulator (formed by 8 hypodermic needles) is placed at an elevation of 120 cm above the soil layer.

Both soil samples were purposely set at the same Cr(VI) concentration of 300 mg kg^{-1} in both the liquid and soild phases, taking into account differences of their initial volumetric water contents (respectively equal to 0.28 and 0.30 for soil 1 and 2) and the preset saturated volumetric water contents (0.49 for both soils), the initial Cr(VI) concentrations (equal to 0 mg kg^{-1} for both soils), and the soil bulk density (1.35 g cm^{-3}). The soils were then packed gradually to a depth of 18.5 cm. The depth of the runoff layer was 1 cm for both experiments. The soil surfaces were covered with plastic films and allowed to incubate for 12 hours. During this time, the system was kept at a constant room temperature of $25°C$. Thus, evaporation from the soil surfaces were considered as negligible. Before the beginning of the rainfall simulation, the outlets of the drainage holes were set to a height of 0 cm for both experiments, i.e., both experiments were conducted under free drainage conditions.

The simulated rainfall was set to an intensity of 0.092 cm min^{-1} and 0.100 cm min^{-1}, respectively for experiments 1 (soil 1) and 2 (soil 2). We denote t_p as the time at which water began ponding on the surface of the soil, t_r and t_s respectively as the times at which runoff first occurred and attained stationarity. Table 2 lists the key parameters characterizing the experimental conditions. Collection of runoff samples was initially performed at 4-10 minutes intervals, progressively longer sampling intervals being used as time elapsed. Dissolved Cr(VI) in the runoff samples were measured by the atomic

flame method using an atomic flame spectrophotometer. Minute quantities of sediments eventually found in the collected water samples were neglected.

Two-layer mathematical model

We rely on the two-layer model for its computational efficiency and because it is grounded on assumptions that are consistent with our experimental conditions. We briefly describe the main characteristics of the two-layer model used in this study, additional details being found in Tong et al. (2010). As shown in Fig. 2, the conceptual model comprised two vertical layers, i.e., the entire mixing zone, that includes the soil mixing layer and the runoff layer, and the underlying soil.

Without considering adsorption, the dissolved chemical mass per unit area, M_w [M L^{-2}], is given by:

$$M_w = C_w\left[\alpha\left(h_w - h_{mix}\theta_s\right) + h_{mix}\theta_s\right] \quad (1)$$

Here, C_w is the aqueous-phase solute concentration in the mixing layer [M L^{-3}]; α ($0 < \alpha \le 1$) is an incomplete mixing coefficient [-]; h_w is the net water depth across the entire mixing zone [L], h_{mix} is the mixing layer thickness [L], and θ_s is saturated volumetric water content in the soil system [L^3 L^{-3}].

In the presence of adsorption, Eq. (1) becomes:

$$M_w = \alpha\left(h_w - h_{mix}\theta_s\right)C_w + h_{mix}\left[\theta_s C_w + \rho_b S\right] \quad (2)$$

where S [M M^{-1}] and ρ_b [M L^{-3}] respectively are the solute concentration adsorbed onto the soil and the soil bulk density.

The dynamic behavior of the system can then be characterized as:

$$\frac{d\left[M_w(t)\right]}{dt} = -\gamma i C_w(t) - \alpha q C_w(t) \quad (3)$$

where γ ($0<\gamma\leq 1$) is an incomplete mixing coefficient [-] (different from α); q [L T^{-1}] and t [T] respectively denoting the specific discharge rate of the overland flow and time.

Adsorption isotherm models

We consider three nonlinear models (i.e., the Langmuir, Freundlich, and Temkin equations) and a linear model to interpret solute adsorption. Given the experimental setting, adsorption is assumed to take place under isothermal conditions.

The Langmuir isothermal nonlinear equation (Langmuir et al., 1918) is:

$$S = S_{\max}\frac{K_{eq}C_w}{1+K_{eq}C_w} \quad (4)$$

where $S_{\max}$ [M M^{-1}] and K_{eq} [L^3 M^{-1}] are (typically unknown and uncertain) model parameters, respectively representing the theoretical maximum adsorption capacity of the soil and the equilibrium adsorption coefficient.

Freundlich et al. (1906) proposed the following empirical nonlinear equation:

$$S = K_f C_w^{\frac{1}{n}} \quad (5)$$

model parameters being the adsorption coefficient K_f [$L^{3/n}$ $M^{-1/n}$] and the exponent n [-]. When n = 1, Eq. (5) reduces to the linear model:

$$S = K_d C_w \quad (6)$$

where K_d [L^3 M^{-1}] is the adsorption coefficient.

The Temkin isotherm model was first proposed by Temkin and Pyzhev (1940) and can be expressed in the form:

$$S = \frac{RT_e}{f}\ln\left(KC_w\right) \tag{7}$$

where R [J mol^{-1} K^{-1}] is the universal gas constant, T_e [K] is absolute temperature, f [J mol^{-1}] is the Temkin isotherm constant, and K [L^3 M^{-1}] is the Temkin isotherm equilibrium binding constant.

Numerical modeling

Embedding each of the adsorption isotherm models (4)-(7) into equations (2)-(3) leads to multiple mathematical models whose relative skill to interpret the observed system behavior is evaluated here. Hereinafter, we denote (*a*) Langmuir, (*b*) Freundlich, (*c*) linear adsorption, or (*d*) Temkin coupled models as the formulations respectively arising by coupling (2)-(3) with (4), (5), (6), or (7). The numerical solution of these solute transport models relies on direct observation of water flow characteristics from the experimental campaign. The observed flow dynamics are then used as input to each transport model and are characterized by segmenting the overall flow process onto the five sequential temporal windows described in the following, each corresponding to a well-defined hydrological manifestation.

Period 0. It comprises observation times ranging from the beginning of the simulated rainfall to the saturation of the mixing layer. During this period, i.e., before the start of water ponding, the water infiltration rate i_{up} [L T^{-1}] coincides with rainfall intensity, p, i.e., $i_{up} = p$ (corresponding to $i = 0$, and $q = 0$). Infiltration from the mixing layer to the underlying soil is assumed to be negligible because the mixing layer is very thin and the time t_{sa} required to attain saturation of the mixing layer can be approximated as:

$$t_{sa} = \frac{h_{mix}\left(\theta_s - \theta_0\right)}{i_{up}} \tag{8}$$

where θ_0 is the initial volumetric water content in the soil system [$M^3\ M^{-3}$].

Period 1. During this period, ranging from saturation of the mixing layer (corresponding to time t_{sa} given by Eq. (8)) to the onset of water ponding, water has not yet ponded on the soil surface, and the infiltration rate of soil equals the rainfall intensity, i.e.:

$$h_w = h_{mix}\theta_s; \qquad i_{up} = i = p; \qquad q = 0 \tag{9}$$

Hereinafter, we illustrate our derivations using the Langmuir isotherm as a test bed, the corresponding derivations associated with the other isotherm models being directly inferable from this. Considering Eqs. (2) and (4) leads to:

$$M_w = \alpha\left(h_w - h_{mix}\theta_s\right)C_w + h_{mix}\left[\theta_s C_w + \rho_s \frac{C_w}{BC_w + C}\right] \tag{10}$$

where $B = 1/S_{\max}$, and $C = 1/\left(K_{eq}S_{\max}\right)$. The initial concentration of the solute in the mixing layer, $C_w\left(t_{sa}\right)$, is obtained from Eq. (10). Replacing Eq. (10) into Eq. (3) yields:

$$\left(h_{mix}\theta_s + \frac{h_{mix}\rho_s}{C}\right)\ln\frac{C_w(t)}{C_w\left(t_{sa}\right)} - \frac{h_{mix}\rho_s}{C}\ln\frac{BC_w(t)+C}{BC_w\left(t_{sa}\right)+C} - \frac{h_{mix}\rho_s}{BC_w(t)+C} + \frac{h_{mix}\rho_s}{BC_w\left(t_{sa}\right)+C} = \gamma p\left(t_{sa} - t\right) \tag{11}$$

We solve Eq. (11) via a fourth-order Runge-Kutta method with a uniform time step of 0.01 seconds.

Period 2. During this window, spanning from the onset of water ponding to the beginning of runoff, respectively observed at experimental times t_p and t_r, the infiltration rate is assumed to decrease linearly in time according to

$i(t) = p - a_0(t - t_p)$, the value of $a_0 > 0$ characterizing the rate of increase of the ponding depth and being evaluated via $i(t_r) = p - a_0(t_r - t_p)$. As no surface runoff is observed, q = 0 during this period and the rate of ponding depth increase equals to $p - i(t)$. The temporal variation of the net water depth of the mixing zone can then be obtained as:

$$h_w = h_p + h_{mix}\theta_s = \frac{1}{2}a_0(t - t_p)^2 + h_{mix}\theta_s \tag{12}$$

where we recall that h_p is the depth of the ponding layer. Concentration $C_w(t_p)$ of the solute in the mixing layer is calculated through Eq. (11) evaluated at time t_p. Combining Eqs. (12), (10), and (3), leads to the following equation describing $C_w(t)$ across this time period:

$$\frac{1}{2}a_0\alpha(t - t_p)^2\frac{\mathrm{d}C_w(t)}{\mathrm{d}t} + a_0\alpha C_w(t)(t - t_p) + h_{mix}\theta_s\frac{\mathrm{d}C_w(t)}{\mathrm{d}t} + \frac{h_{mix}\rho_s C}{\left[BC_w(t) + C\right]^2}\frac{\mathrm{d}C_w(t)}{\mathrm{d}t} = \gamma\left[a_0(t - t_p) - p\right]C_w(t) \tag{13}$$

Similar to Eq. (11), we solve Eq. (13) via a fourth-order Runge-Kutta method with a uniform time step of 0.01 seconds.

Period 3. During this interval, ranging from the onset of runoff to its stabilization (at time t_s), the temporal decrease of infiltration is approximated via:

$$i(t) = i(t_r) - b(t - t_r); \qquad q = p - i \tag{14}$$

where *b* is a parameter characterizing the infiltration decrease rate and is evaluated via $i(t_s) = i(t_r) - b(t_s - t_r)$. The initial solute concentration in the runoff fluid, $\alpha C_w(t_r)$, can be obtained from the solution of Eq. (13), evaluated at time *t* = t_r. Substituting Eqs. (14) and (10) into Eq. (3) yields:

$$\left[\alpha h_p + h_{mix}\theta_s\right]\ln\frac{C_w(t)}{C_w(t_r)} + \frac{h_{mix}\rho_s}{C}\ln\frac{C_w(t)}{C_w(t_r)} - \frac{h_{mix}\rho_s}{C}\ln\frac{BC_w(t)+C}{BC_w(t_r)+C} - \frac{h_{mix}\rho_s}{BC_w(t)+C} + \frac{h_{mix}\rho_s}{BC_w(t_r)+C} = \left\{(\alpha-\gamma)\left[i(t_r)+bxt_r\right]-\alpha p\right\}t - t_r - \frac{b}{2}(\alpha-\gamma)\left(t^2-t_r^2\right) \quad (15)$$

A fourth-order Runge-Kutta method is employed to solve Eq. (15) with the same time step as in the previous time periods.

Period 4. The infiltration rate is stationary during this last period and can be obtained by evaluating Eq. (14) at time $t = t_s$. The initial concentration of the runoff fluid, $\alpha C_w(t_s)$, is obtained by evaluating Eq. (15) at time $t = t_s$. The resulting format of Eq. (3), i.e.:

$$\left[\alpha h_p + h_{mix}\theta_s\right]\ln\frac{C_w(t)}{C_w(t_r)} + \frac{h_{mix}\rho_s}{C}\ln\frac{C_w(t)}{C_w(t_r)} - \frac{h_{mix}\rho_s}{C}\ln\frac{BC_w(t)+C}{BC_w(t_r)+C} - \frac{h_{mix}\rho_s}{BC_w(t)+C} + \frac{h_{mix}\rho_s}{BC_w(t_r)+C} = \left[i(t_s)(\alpha-\gamma)-\alpha p\right](t-t_s) \quad (16)$$

is then solved by a fourth order Runge-Kutta method, as described above.

For brevity, the solute transport models obtained by considering the Langmuir, Freundlich, Temkin and linear adsorption models are respectively denoted as L, F, T and H models.

Maximum Likelihood Model calibration

We consider the vector $\mathbf{Y}^* = [Y^*_{(1)}, Y^*_{(2)}, \cdots, Y^*_{(N_C)}]$ collecting N_C measurements of dissolved Cr(VI) concentration observed in surface the runoff at sampling time i = 1, 2, ..., N_C. The general relationship expressing Cr(VI) concentration in runoff through a mathematical model $f(.)$ associated with the vector $\mathbf{X} = [x_1, x_2, \cdots, x_{N_p}]$ of N_P unknown parameters is here represented as $\mathbf{Y} = f(\mathbf{X})$, vector $\mathbf{Y} = [Y_{(1)}, Y_{(2)}, \cdots, Y_{(N_C)}]$ including N_C simulated Cr(VI) concentration values in the runoff at time i = 1, 2, ...,

N_C. Experimental measurement errors are considered to be independent (e.g., Carrera and Neuman, 1986; Bianchi-Janetti et al., 2012), the corresponding error covariance matrix, $\mathbf{B}_C$, being diagonal, σ_i^2 (i = 1, 2, ..., N_C) representing observation error variance. The Maximum Likelihood (ML) estimate $\hat{\mathbf{X}}$ of the vector of the N_P uncertain model parameters can be obtained by minimizing with respect to $\mathbf{X}$ the negative log likelihood criterion (e.g., Carrera and Neuman 1986):

$$\mathrm{NLL} = \sum_{i=1}^{N_C} \frac{Y_{(i)}^* - \hat{Y}_{(i)}}{\sigma_i^2} + \ln\left|\mathbf{B}_\mathrm{C}\right| + N_C \ln(2\pi) \tag{17}$$

where $\hat{Y}_{(i)}$ is the output provided by a given interpretive model at the i^{th} observation time. We note that minimizing Eq. (17) corresponds to minimization of the least square criterion (Carrera and Neuman, 1986; Bianchi-Janetti et al., 2012 and references therein):

$$J = \sum_{i=1}^{N_C} \frac{Y_{(i)}^* - \hat{Y}_{(i)}}{\sigma_i^2} \tag{18}$$

Here, minimization of (18) is obtained upon relying on the iterative Levenberg-Marquardt algorithm as embedded in the well documented computational framework PEST (Doherty, 2002). We consider minimizing Eq. (18) with uniform (and generally unknown) measurement error variance, i.e., $\sigma_i^2 = \sigma^2$ for i = 1, 2, ..., N_C (see, e.g., Bianchi-Janetti et al., 2012).

Model Identification Criteria

To evaluate the performance of the four alternative models considered (i.e., L, F, T and H), we rely on the four criteria:

$$\mathrm{AIC} = \mathrm{NLL} + 2N_P \tag{19}$$

$$\mathrm{AIC_C} = \mathrm{NLL} + 2N_P + \frac{2N_P\left(N_P+1\right)}{N_C - N_P - 2} \tag{20}$$

$$\mathrm{BIC} = \mathrm{NLL} + N_P \ln(N_C) \tag{21}$$

$$\mathrm{KIC} = \mathrm{NLL} + N_P \ln\left(\frac{N_C}{2\pi}\right) - \ln\left|\mathbf{Q}\right| \tag{22}$$

where **Q** represents the Cramer-Rao lower-bound approximation for the covariance matrix of the parameter estimates, i.e., the inverse expected Fisher information matrix, which renders a quantitative appraisal of the quality of parameter estimates and of the information content carried by data about model parameters (see, e.g., Ye et al., 2008 for details). Here, Eq. (19) is proposed by Akaike (1974), Eq. (20) by Hurvich and Tsai (1989), Eq. (21) by Schwartz (1978) and Eq. (22) by Kashyap (1982). It is noted that the lowest value of a given model identification criterion indicates the most favored model (according to the criterion itself) at the expense of the other ones.

Maximum Likelihood Bayesian Modeling averaging

The discrimination criteria (19)-(22) can also be considered to assign posterior probability weights quantifying uncertainty associated with each of the tested isotherm models. The posterior probability linked to model M_k (k = 1, 2, ..., N_M, N_M, which is equal to 4 in our study, being the number of interpreting models assessed) is evaluated as (Ye et al., 2008):

$$P\left(M_k \mid \mathbf{Y}^*\right) = \frac{\exp\left(-\frac{1}{2}\left(IC_k - IC_{\min}\right)\right)P\left(M_k\right)}{\sum_{k}^{N_M}\exp\left(-\frac{1}{2}\left(IC_k - IC_{\min}\right)\right)P\left(M_k\right)} \tag{23}$$

where IC_k is either AIC (19), $\mathrm{AIC_C}$ (20), BIC (21), or KIC (22), IC_{min} = min$\{IC_k\}$ being its minimum value calculated across the set of the four models examined; and

379 $P(M_k)$ is the prior probability associated with the k^{th} alternative model. Because no
380 prior information is available, we set $P(M_k) = 1/N_M$.

381 Averaging across the moments provided by all alternative models renders the
382 following (Bayesian-averaged) expressions for the leading moments (Draper, 1995;
383 Hoeting et al., 1999):

384 $$E(\mathbf{Y} \mid \mathbf{Y}^*) = \sum_{k=1}^{N_M} E(\mathbf{Y} \mid \mathbf{Y}^*, M_k) P(M_k \mid \mathbf{Y}^*) \quad (24)$$

385 $$V(\mathbf{Y} \mid \mathbf{Y}^*) = \sum_{k=1}^{N_M} Var(\mathbf{Y} \mid \mathbf{Y}^*, M_k) P(M_k \mid \mathbf{Y}^*) + \sum_{k=1}^{N_M} \left(E(\mathbf{Y} \mid \mathbf{Y}^*, M_k) - E(\mathbf{Y} \mid \mathbf{Y}^*) \right)^2 P(M_k \mid \mathbf{Y}^*) \quad (25)$$

386 Here, $E(\mathbf{Y} \mid \mathbf{Y}^*)$ and $V(\mathbf{Y} \mid \mathbf{Y}^*)$ respectively are model-averaged estimate and
387 variance of $\mathbf{Y}$ conditional on the set of Cr(VI) observations collected in $\mathbf{Y}^*$; and
388 $E(\mathbf{Y} \mid \mathbf{Y}^*, M_k)$ and $V(\mathbf{Y} \mid \mathbf{Y}^*, M_k)$ respectively are the mean and variance of $\mathbf{Y}$
389 conditional on $\mathbf{Y}^*$ and model M_k.

390

391 ## RESULTS AND DISCUSSION

392 Here, we start by illustrating the available Cr(VI) observations and discuss the results
393 of ML-based calibration of the four models analyzed. We then quantify posterior model
394 weights according to the selection criteria considered and use these to (*a*) rank the
395 models in terms of their relative skill to interpret the available data and (*b*) compute
396 model-averaged estimates and corresponding uncertainty bounds. We resort to a
397 classical variance-based global sensitivity analysis (GSA) to quantify the relative
398 contribution of the uncertain parameters characterizing each of the models tested to the

399 variability of Cr(VI) concentration in the runoff water. We then discuss the implication
400 of adsorption function by relying on the most skillful amongst the models tested to
401 characterize Cr(VI) loss from soil to surface runoff.

402 *Model ranking*

403 Observed Cr(VI) concentrations in the runoff for experiments 1 and 2 are
404 respectively depicted in Fig. 3a and 3b. These figures depict the corresponding
405 concentration values obtained after ML model calibration for the four models analyzed.
406 Table 3 lists ML parameter estimates together with the associated standard deviation
407 (SD).

408 Simulated concentrations are generally in good agreement with experimental
409 evidences, a remarkable exception being model T in experiment 1. The high values of
410 the estimated standard deviations listed in Table 3 can be partially due to linearity
411 assumptions upon which the employed parameter optimization strategy is implemented
412 and/or a trade-off between the information content associated with data and the number
413 and nature of model parameters considered (Doherty 2002). The latter observation is
414 consistent with the observed high values of the entries of the cross-correlation matrix
415 associated with parameter estimates. These are listed in Table 4 and suggest that the
416 available data are not conducive to unique estimates of model parameters.

417 Model calibration results indicate that the soil used in experiment 2 has a higher
418 adsorption capacity than the soil in experiment 1. This result is consistent with the
419 experimental setting, which comprises a finer soil texture in experiment 2. One can also
420 note that experiment 2 is associated by a higher depth of the mixing layer than
421 experiment 1. This finding is consistent with our experiment setting, according to which

soil 1 can form a much stronger shield (Heilig et al., 2001) against rain drop erosion on surface soil 1 than soil 2, because of its sedimentological composition. This partially supports the higher Cr(VI) concentrations obtained for experiment 2, which are consistent with the observation that the depth of the mixing layer directly influences the total mass of solute that can be transferred from soil to surface runoff. One should also notice that a higher infiltration rate occurs in experiment 1 than in experiment 2, thus indirectly suggesting that less Cr(VI) mass is lost in the mixing layer through surface runoff in the former set-up than in the latter.

Calculated values for each of the model identification criteria considered are listed in Table 5. We can see that AIC, AIC_C and BIC values are close, because of their similar structures. For experiment 1, the lowest AIC, AIC_C, BIC and KIC values are -140.79, -137.46, -134.90, and -156.22, respectively, their corresponding counterparts for experiment 2 being -36.04, -30.79, -29.23, and -61.81, respectively. Posterior model weights of the alternative models analyzed are listed in Table 6. For experiment 1, the highest AIC-, AIC_C- and BIC-based posterior model weights are 47.09%, 66.54% and 61.60%, respectively, all of them being associated with the H model. Otherwise, the highest KIC-based posterior model weight (i.e., 53.97%) is linked to the L model. For experiment 2, the highest AIC-, AIC_C- and BIC-based posterior model weights are 90.39%, 90.30% and 90.34%, respectively, all of them being connected to the L model. The highest KIC-based posterior model weight is 77.87% and is linked to the T model. One can then conclude that the H and/or L model are identified as the most skillful ones for experiment 1, respectively according to the BIC- and/or KIC-based posterior model

444 weights, the L and/or T models being favored to the interpretation of experiment 2.

445 According to Ye et al. (2008), AIC and AIC_C are based on the premise that the true
446 model is comprised in the set of alternative models tested, a constraint which is not
447 shared by BIC or KIC. Additionally, it can be noted that KIC imbues a balancing effect
448 between expected value of information and model parsimony. At the same time, it has
449 been observed that KIC tends to favor models which can lead to potentially
450 controversial results, due to the effect of **Q** (e.g., Tsai and Li, 2008; Li and Tsai, 2009).
451 On the basis of this discussion, and for the purpose of our application, we base our
452 model selections on KIC. By further noting that the T model displays an unsatisfactory
453 pattern in the interpretation of experiment 1 (see Fig. 3a), we conclude that the L model
454 can be considered as the most skillful amongst the alternatives considered for the
455 purpose of the overall interpretation of both experimental datasets.

456 We now illustrate the results of the MLBMA multi-model analysis. The latter is
457 performed through a numerical Monte Carlo (MC) framework structured according to
458 the following steps: (*a*) N = 100,000 MC samples of each uncertain model parameter
459 x_i ($i = 1, 2, \cdots, N_P$) are randomly generated for each candidate model M_k
460 ($k = 1, 2, \cdots, N_M$) through the Latin Hypercube sampling technique considering each
461 x_i as independent and identically distributed (i.i.d.) random variables, uniformly
462 distributed within the support $\left[\hat{x}_i - 30\%\hat{x}_i,\ \hat{x}_i + 30\%\hat{x}\right]$, with mean value equal to $\hat{x}_i$
463 (i.e., the ML-based parameter estimate); (*b*) calculating N MC realizations of dissolved
464 Cr(VI) concentrations in the surface runoff (collected in vector **Y**) via each candidate
465 model M_k ; (*c*) computing (ensemble) mean $E\left(\mathbf{Y} \mid \mathbf{Y}^*, M_k\right)$ and variance

466 $V\left(\mathbf{Y}\,|\,\mathbf{Y}^*, M_k\right)$; (*d*) and evaluating model-averaged estimates $E\left(\mathbf{Y}\,|\,\mathbf{Y}^*\right)$ and
467 $Var\left(\mathbf{Y}\,|\,\mathbf{Y}^*\right)$ through (25) and (26).

468 Fig. 4 depicts scatterplots of model-averaged estimates $E\left(\mathbf{Y}\,|\,\mathbf{Y}^*\right)$ and
469 corresponding uncertainty bounds (of width equal to $\pm\sqrt{V\left(\mathbf{Y}\,|\,\mathbf{Y}^*\right)}$) versus Y
470 measurements for experiment 1 on the basis of *IC* = AIC (Fig. 4a), AIC_C (Fig. 4b), BIC
471 (Fig. 4c), and KIC (Fig. 4d). For completeness, each subplot also depicts
472 $E\left(\mathbf{Y}\,|\,\mathbf{Y}^*, \tilde{M}_k\right)$ and $E\left(\mathbf{Y}\,|\,\mathbf{Y}^*, \tilde{M}_k\right) \pm \sqrt{V\left(\mathbf{Y}\,|\,\mathbf{Y}^*, \tilde{M}_k\right)}$, as computed by the most
473 skillful model, $\tilde{M}_k$, identified by the corresponding *IC*. Maximum Likelihood
474 estimates of Y obtained through model $\tilde{M}_k$ (with corresponding model parameter
475 set $\hat{\mathbf{X}}$) are also depicted. Values of the highest posterior model weights, $P\left(\hat{M}_k\,|\,\mathbf{Y}^*\right)$,
476 are also included in each subplot. Corresponding depictions for experiment 2 are shown
477 in Fig. 5.

478 These results suggest that: (*i*) $E\left(\mathbf{Y}\,|\,\mathbf{Y}^*\right)$ and $E\left(\mathbf{Y}\,|\,\mathbf{Y}^*\right) \pm \sqrt{V\left(\mathbf{Y}\,|\,\mathbf{Y}^*\right)}$ are
479 respectively very close to $E\left(\mathbf{Y}\,|\,\mathbf{Y}^*, \tilde{M}_k\right)$ and $E\left(\mathbf{Y}\,|\,\mathbf{Y}^*, \tilde{M}_k\right) \pm \sqrt{V\left(\mathbf{Y}\,|\,\mathbf{Y}^*, \tilde{M}_k\right)}$
480 when $P\left(\hat{M}_k\,|\,\mathbf{Y}^*\right) \geq 90\%$ (see Fig. 5); (*ii*) $E\left(\mathbf{Y}\,|\,\mathbf{Y}^*\right)$ can provide better estimates
481 than $E\left(\mathbf{Y}\,|\,\mathbf{Y}^*, \tilde{M}_k\right)$ when the individual models of the set considered yield very
482 different results (see Fig. 4); (*iii*) the KIC-based $Var\left(\mathbf{Y}\,|\,\mathbf{Y}^*, \tilde{M}_k\right)$ is always smaller
483 than its counterparts based on the other *IC* considered for a given experiment (see Figs.
484 4 and 5). These results are consistent with observations by Ranaee et al. (2016), who
485 noted that model-averaged estimates were virtually coinciding with those associated
486 with the most skillful model in their study when the latter was characterized by
487 $P\left(\hat{M}_k\,|\,\mathbf{Y}^*\right) \geq 95\%$. They are also consistent with the results of Winter and Nychka

488 (2010), who note that a model average can only be more skillful than the model
489 identified as best solely when the individual models in the collection produce very
490 different forecasts.

491 Figs. 6 and 7 complement the results illustrated above by depicting the Monte Carlo
492 based probability density functions (*pdfs*) of Cr(VI) concentration in the water runoff
493 evaluated through the candidate models, respectively for experiments 1 and 2. Results
494 are illustrated for early (T_1), median (T_2), and late (T_3) simulation times, respectively
495 corresponding to sampling times when observations $Y^*_{(i)}$ (i = 1, 5, and 23) are collected.
496 One can see that the densities calculated by the L model generally peak at a value
497 closely corresponding to the measured Cr(VI) concentration, an exception being given
498 by the late times results of Fig. 6c, where the *pdfs* associated with the H and L models
499 resemble a Delta function. The *pdfs* associated with F and H models generally show
500 higher skewness and heavier tails, which partially indicate increased probability of
501 extreme values, in comparison with L and T models.

502 *Variance-based global sensitivity analysis*

503 We provide further insights on the way that model uncertain parameters can
504 contribute to the variability of model responses through a sensitivity analysis. In this
505 context, local sensitivity analysis approaches (*i*) quantify the sensitivity of a model
506 output to small perturbations of parameter values and (*ii*) provide an appraisal of the
507 behavior of the modeled system in regions of the parameter space close to the perturbed
508 value of the parameter (e.g., Razavi and Gupta, 2015 and references therein). GSA
509 techniques enable us to evaluate sensitivities of model outputs across the overall

support defining the space of variability of model parameters (e.g., Formaggia et al., 2013; Ciriello et al., 2013, 2015; Riva et al., 2015; Razavi and Gupta, 2015, Dell'Oca et al., 2017 and references therein). The latter is based on the evaluation of the Sobol' indices, which are based on a classical decomposition of variance and provide information on the relative contribution of each uncertain model parameter to the variance of a target model output. Here, we apply the variance-based GSA approach (Saltelli et al., 2008; 2010).

Evaluation of the variance-based sensitivity indices is performed by considering uncertain model parameters as independently random variables, within the space of variability described above. The total sensitivity indices for the i^{th} model parameter (or factor) corresponding to the j^{th} Cr(VI) measurement in the runoff is evaluated as (Saltelli et al., 2008, 2010)

$$S_{T(ij)} = 1 - \frac{V(E(Y_{(j)} \mid x_1, x_2, \cdots, x_{i-1}, x_{i+1}, \cdots, x_{N_p}))}{V(Y_{(j)})} = \frac{E(V(Y_{(j)} \mid x_1, x_2, \cdots, x_{i-1}, x_{i+1}, \cdots, x_{N_p}))}{V(Y_{(j)})} \quad (25)$$

Here, $V(Y_{(j)})$ is the variance of model response at the time corresponding to the j^{th} Cr(VI) observation in the runoff; $V(E(Y_{(j)} \mid x_1, x_2, \cdots, x_{i-1}, x_{i+1}, \cdots, x_{N_p}))$ represents the variance of model responses expectation conditioned to all factors, excluding factor x_i; $E(V(Y_{(j)} \mid x_1, x_2, \cdots, x_{i-1}, x_{i+1}, \cdots, x_{N_p})) = 1 - V(E(Y_{(j)} \mid x_1, x_2, \cdots, x_{i-1}, x_{i+1}, \cdots, x_{N_p}))$ is the expected variance conditioned on all factors, excluding factor x_i. In our study, $E(V(Y_{(j)} \mid x_1, x_2, \cdots, x_{i-1}, x_{i+1}, \cdots, x_{N_p}))$ is evaluated through Eq. (19) in Saltelli et al. (2010). We note that Sobol' total sensitivity indices are informative of the relative importance of each model input to the variance of model output and are not amenable

to interpretations leading to ranking of the relative interpretive skill of the collection of models considered.

We illustrate our results of GSA for the setting of experiment 2. Figs. 8-11 depict the temporal pattern displayed by $S_{T(ij)}$ as a function of the size, *N*, of the collection of random parameter values for the models tested. These results suggest that N = 5000 samples yields sufficiently stable results.

Fig. 12 depicts the temporal variation of the contribution (quantified by $S_{T(ij)} / \sum_{i=1}^{N_P} S_{T(ij)} \times 100\,\%$) of each input factor to model output for all candidate models. These results indicate that model output *Y* is most sensitive to h_{mix} for all alternative models, and are consistent with the observation that the depth of the mixing layer directly determines the mass of Cr(VI) that could be transported from soil to surface runoff. An exception to this pattern is given by model F whose model output is very sensitive to parameter *n*, which is mainly due to the importance of *n* to drive the power law behavior in Eq. (5). Results in Fig. 12 suggest that the sum of the contributions associated with the adsorption parameters consistently increases as simulation time progresses for all models. Considering model L as an example, the contributions of K_{eq} and $S_{\max}$ are respectively 0.47% and 1.38% at the beginning simulation, and increase up to 6.61% and 24.02% at the end of simulation. This corresponds to an increase of the combined total contributions of K_{eq} and $S_{\max}$ to σ_Y^2 from 1.85% to 30.63% during the simulation period and denote the significant effect of the adsorption process on Cr(VI) loss from soil to the surface runoff, especially at late times.

Fig. 12 also suggests that the parameters with the lowest (in an average sense)

553 contribution to σ_Y^2 are K_{eq} (for model L), α (for models F and H), and K_t (for
554 model T). We denote here as $C_{T(K_{eq})}$ = 5.41%, $C_{T(\alpha_F)}$ = 2.33%, $C_{T(\alpha_H)}$ = 10.41%,
555 and $C_{T(K_t)}$ = 0.00%, the average of the temporal contributions evaluated for each of
556 these parameters over the set of 23 observation times in experiment 2. It is interesting
557 to note that the ranking $C_{T(K_t)} < C_{T(\alpha_F)} < C_{T(K_{eq})} < C_{T(\alpha_H)}$ is somehow consistent with the
558 ranking of posterior model weights based on KIC (i.e., 77.87%, 17.76%, 4.37% and
559 0.00%, respectively for models T, F, L and H; see Table 6).

560 As a complement to these results, Fig. 13 depicts the temporal variation of the
561 quantity $\frac{1}{N_p}\sum_{i=1}^{N_p}\left|S_{T(ij)} - S_{1(ij)}\right|$, representing the mean of absolute difference between the
562 total ($S_{T(ij)}$) and first-order ($S_{1(ij)}$) sensitivity indices. As a remark, one can see that low
563 values of this quantity typically correspond to high KIC-based posterior model weights,
564 with the exception of model T in experiment 1. This finding might be considered as an
565 indication that low values of $\frac{1}{N_p}\sum_{i=1}^{N_p}\left|S_{T(ij)} - S_{1(ij)}\right|$ can be consistent with the low
566 expected Fisher information. Additional theoretical developments are needed to fully
567 explore possible implications of these results and will be the subject of future
568 investigations.

569 *Effect of adsorption on Cr(VI) loss from soil to surface runoff*

570 While global sensitivity analyses of the kind we illustrate provide global measures
571 quantifying the contribution of uncertain input parameters to the variance of a model
572 output *pdf* across the entire investigated parameter space, they do not yield a
573 straightforward assessment of (*a*) the actual values attained by model outputs within

574 the parameter space or (*b*) the direction of variation of model results as a function of
575 parameter variation. These features can be readily visualized through a scatterplot
576 analysis. We illustrate the results of the latter by considering the L model, which has
577 been ranked as best in our prior analyses.

578 Figs. 14 and 15 depict the data clouds associated with the scatterplots of Cr(VI)
579 concentrations in the water runoff resulting from the L model at sampling times
580 respectively corresponding to the collection of the first and last concentration
581 measurement (i.e., Y_1^* and $Y_{N_C}^*$) in experiment 2. Linear regression curves are also
582 depicted for completeness.

583 These results generally indicate that *Y* is positively correlated to α and negatively
584 correlated to γ. They are consistent with the definition of $Y = \alpha C_w$ and with the
585 observation that a strong incomplete mixing (associated with high values of the mixing
586 coefficient γ) results in decreased values of Cr(VI) in the water runoff (i.e., an
587 increased transfer of Cr(VI) from the mixing layer to the underlying soil). The positive
588 correlation of *Y* with the depth of the mixing layer h_{mix} (Figs. 14e, and 15e) stems
589 from the physical effects of the mixing layer.

590 The correlation between *Y* and the adsorption parameter $S_{\max}$ changes from
591 negative to positive with elapsing time (compare Figs. 14d and 15d). At the beginning
592 of the simulation period, high values of $S_{\max}$ tend to increase the total Cr(VI) mass
593 adsorbed onto the solid phase with a decrease of the mass released to runoff. As time
594 progresses, the dissolved Cr(VI) concentration in the mixing layer decreases, promoting
595 desorption from the solid and subsequent transfer to runoff. These results are also

596 consistent with the tailing observed for the breakthrough curve of Cr(VI) for experiment
597 1.
598

599 ## CONCLUSIONS

600 The results from two experiments are used to investigate Cr(VI) losses from soils
601 with diverse grain sizes to water runoff. Four solute transport models (denoted as L, F,
602 T and H), coupling a two-layer solute transfer model, respectively, with Langmuir,
603 Freundlich, Temkin, and linear adsorption isotherms, are assessed to simulate Cr(VI)
604 transfer from soil to surface runoff. Each of the analyzed models is calibrated against
605 experimental data through Maximum Likelihood (ML) parameter estimation. Four
606 model identification criteria (i.e., AIC, AIC_C, BIC and KIC) are evaluated, and posterior
607 probabilistic weights are then calculated to identify the most skillful model to interpret
608 the available data. The classical variance-based global sensitivity and scatterplot
609 sensitivity analyses are then performed in the context of both experimental settings. Our
610 study leads to the following key conclusions.

611 (1) Cr(VI) concentrations in the runoff are much higher in experiment 2 than in
612 experiment 1. The most significant difference between the two experimental
613 scenarios is the soil grain size (i.e., soils were sieved through 2 mm and 1 mm sieves
614 for experiments 1 and 2, respectively). This result can be explained by two
615 mechanisms: (*a*) larger grain sizes would increase infiltration rates; and (*b*) a mixing
616 layer depth tends to be decreased in a soil with larger grain size, resulting in a

617 decreased Cr(VI) loss through runoff.

618 (2) For experiment 1, the largest AIC, AIC_C and BIC-based posterior model weights
619 are associated with model H, respectively with values of 47.09%, 66.54% and
620 61.60%. Model L is ranked highest by KIC, with a posterior weight of 53.97%. For
621 experiment 2, the highest AIC, AIC_C and BIC-based posterior model weights are
622 90.39%, 90.30% and 90.34%, respectively, and are linked to model L; Model T is
623 favored by KIC, with a posterior weight equal to 77.87%. Model L is then evaluated
624 as the most skillful for the overall interpretation of both experimental results.

625 (3) Variance-based global sensitivity results suggest that the thickness of the mixing
626 layer, h_{mix}, is the most sensitive parameter for all models, an exception being the
627 Freundlich model, where *n* is the uncertain parameter with the highest contribution
628 to the model output variance. The total sensitivity of the adsorption parameters
629 tends to increase with simulation time. For example, in the case of model L the sum
630 of the K_{eq} and $S_{\max}$ contributions (see Fig. 12b) to model output variance
631 increases from 1.85% to 30.63% across the temporal window spanned in
632 experiment 2. This result suggests that adsorption has a significant effect on the
633 uncertainty of prediction for Cr(VI) loss from soil to runoff.

634 (4) The scatterplot analysis results from model L suggest that the incomplete mixing
635 coefficient (α) and the depth of mixing layer (h_{mix}) are positively correlated with
636 Cr(VI) concentration in the runoff, and the incomplete mixing coefficient (γ) and
637 Cr(VI) concentration are negatively correlated. The correlation between Cr(VI)
638 concentration in the runoff and the maximum adsorption capacity ($S_{\max}$) changes

639 from negative to positive during the simulation process. These results are obtained
640 from the finding that (*a*) large values of S_{max} tend to increase the total Cr(VI) mass
641 adsorbed onto the solid phase at the beginning of the simulation period; and (*b*) the
642 dissolved Cr(VI) concentration in the mixing layer decreases as time progresses,
643 promoting Cr(VI) transfer from soil to runoff.

644 It is remarked that the mathematical formulation for the adsorption process plays a
645 significant role on prediction of solute loss from soil to surface water runoff, and the
646 equilibrium adsorption assumption is not accurate in some field scenarios. Non-
647 equilibrium adsorption models should be further explored in future studies when they
648 are used in the two-layer model to describe chemical transport from soil to water runoff.

649 Additional elements of future study should also include the use of global sensitivity
650 techniques that allow exploring the relative importance of each uncertain model
651 parameter through the evaluation of (statistical) Moment-based Metrics of the kind
652 proposed by Dell'Oca et al. (2017). The latter are not confined to a description of the
653 feedback between uncertain model inputs and outputs via variance-based metrics (such
654 as the Sobol' indices) and aim at providing a comprehensive picture, quantifying the
655 impact of model parameter uncertainties on the statistical moments driving the main
656 features of the probability density function of model outputs.

657

658 **ACKNOWLEDGMENTS**

659 This work was partly supported by the National Natural Science Foundation of China
660 (Grant No. 41530316, 51209187, 91125024), and the National Key Research and
661 Development Program of China (Grant No. 2016YFC0402805). The authors are

grateful to Professor Jinzhong Yang for his assistance and dedication during the laboratory experiments. Funding from MIUR (Italian ministry of Education, University and Research, Water JPI, Water Works 2014, Project: WE-NEED- Water NEEDs, availability, quality and sustainability) is also acknowledged.

We thank Editor John L. Nieber and the three anonymous reviewers for their constructive comments.

REFERENCES

Akaike H. 1974. A new look at statistical model identification. IEEE Transactions on Automatic Control, 19: 716-723.

Ahuja LR, Sharpley AN, Yamamoto M, Menzel RG. 1981. The depth of rainfall-runoff-soil interaction as determined by 32P. *W*ater *Resources Research*, 17(4): 969-974.

Ahuja LR, Lehman OR. 1983. The extent and nature of rainfall soil interaction in the release of soluble chemicals to runoff. *Journal of Environmental Quality*, 12(1): 34-40.

Apte AD, Verma S, Tare V and Bose P. 2005. Oxidation of Cr(III) in tannery sludge to Cr(VI): field observations and theoretical assessment. *Journal of Hazardous Materials*, 121(1-3): 215.

Bianchi-Janetti E, Dror I, Riva M, Guadagnini A and Berkowitz B. 2012. EstimationofSingle-MetalandCompetitiveSorptionIsothermsthroughMaximumLikelihoodandModelQualityCriteria. *Soil Science Society of America Journal*, 76: 1229-1245.

Carrera J and Neuman SP. 1986. Estimation of aquifer parameters under transient and steady state conditions: 1. Maximum likelihood method incorporating prior

686 information. *Water Resources Research*, 22(2): 199-210.
687 Chakraborty R, Ghosh A, Ghosh S, Mukherjee S. 2015. Evaluation of contaminant
688 transport parameters for hexavalent chromium migration through saturated soil media.
689 *Environmental Earth Science*, 74: 5687-5697.
690 Ciriello V, Edery Y, Guadagnini A, and Berkowitz B. 2015. Multimodel framework for
691 characterization of transport in porous media, *Water Resources Research*, 51(5): 3384-
692 3402.
693 Ciriello V, Di Federico V, Riva M, Cadini F, De Sanctis J, Zio E, and Guadagnini A.
694 2013. Polynomial chaos expansion for global sensitivity analysis applied to a model
695 of radionuclide migration in a randomly heterogeneous aquifer, *Stochastic*
696 *Environmental Research and Risk Assessment*, 27: 945-954.
697 Dell'Oca A, Riva M, Guadagnini A. 2017. Moment-based Metrics for Global
698 Sensitivity Analysis of Hydrological Systems. *Hydrology and Earth System Sciences*,
699 21: 6219-6234.
700 Donigian AS, Jr, Beyerlein DC, Davis HH, Crawford NH. 1977. Agricultural runoff
701 management (ARM) model, version II; Refinement and testing. EPA 600/3-77-098.
702 Environ. Res. Lab. U.S. EPA, Athens, Ga. U.S. Government Printing Office,
703 Washington, D.C.
704 Draper, D. 1995. Assessment and propagation of model uncertainty, *Journal of the*
705 *Royal Statistical Society: Series B*, 57(1): 45 - 97.
706 Doherty J. 2002. PEST: Model in dependent parameter estimation, user manual. 4thed.
707 Watermark Numer. Computing, Corinda, Queensland.

Dong WC, Wang QJ. 2013. Modeling Soil Solute Release into Runoff and Transport with Runoff on a Loess Slope. *Journal of Hydrologic Engineering*, 18: 527-535.

Fifi U, Winiarski T, Emmanuel E. 2013. Assessing the Mobility of Lead, Copper and Cadmium in a Calcareous Soil of Port-au-Prince, Haiti. *International Journal of Environmental Research and Public Health*, 10(11): 5830-5843.

Formaggia L, Guadagnini A, Imperiali I, Lever V, Porta G, Riva M, Scotti A, and Tamellini L. 2013. Global sensitivity analysis through polynomial chaos expansion of a basin-scale geochemical compaction model, *Computational Geosciences*, 17: 25-42.

Freundlich HMF. 1906. Over the adsorption in solution. *zeitschrift fur physikalische chemie-international journal of research in physical chemistry & chemical physics*, 57: 385-470.

Fendorf SE. 1995. Surface reactions of chromium in soils and waters. Geoderma 67: 55-71.

Fendorf SE, Zasoski RJ. 1992. Chromium(III) oxidation by & MnO, I: Characterization. *Environmental Science &Technology*, 26: 79-85.

Gao B, Walter MT, Steenhuis TS, Hogarthb WL, Parlange J-Y. 2004. Rainfall induced chemical transport from soil to runoff: theory and experiments. *Journal of Hydrology*, 295(1-4): 291-304.

Ghosh S, Mukherjee S; Sarkar K, Al-Hamdan A.M. ASCE Ashraf Z., Krishna R. Reddy, F. ASCE. 2012. Experimental Study on Chromium Containment by Admixed Soil Liner. Journal of environmental engineering, 137: 1048-1057.

Gupta S, Bahu BV. 2009. Modeling, simulation, and experimental validation for

730 continuous Cr(VI) removal from aqueous solutions using sawdust as an adsorbent.
731 *Bioresource Technology*, 100: 5633-5640.
732 Hurvich CM and Tsai CL. 1989. Regression and time series model selection in small
733 sample. *Biometrika*, 76(2): 297-307.
734 Hairsine PB, Rose CW. 1991. Rainfall detachment and deposition: sediment transport
735 in the absence of flow-driven processes. *Soil Science Society of America Journal*, 55:
736 320-324.
737 Hoeting JA, Madigan D, Raftery AE, and Volinsky CT. 1999. Bayesian model
738 averaging: A tutorial, *Statistical Science*., 14(4): 382-417.
739 Heilig A, Debruyn D, Walter MT, Rose CW, Parlange J-Y, Steenhuis TS, Sander GC,
740 Hairsine PB, Hogarth WL, Walker LP. 2001. Testing of a mechanistic soil erosion
741 model with a simple experiment. *Journal of Hydrology*, 244(1-2): 9-16.
742 He ZL, Zhang MK, Calvert DV, Stoffella PJ, Yang XE, Yu S. 2004. Transport of heavy
743 metals in surface runoff from vegetable and citrus Fields. *Soil Science Society of*
744 *America Journal*, 68: 1662-1669.
745 Kashyap RL. 1982. Optimal choice of AR and MA parts in autoregressive moving
746 average models. *IEEE Transactions on Pattern Analysis & Machine Intelligence*, 4(2):
747 99-104.
748 Krishna AK, Govil PK. 2008. Assessment of heavy metal contamination in soils around
749 Manali industrial area, Chennai, Southern India. *Environmental Geology*, 54(7):
750 1465-1472.
751 Langmuir I. 1918. The adsorption of gases on plane surfaces of glass, mica and Pt.

752 *Journal of the American Chemical Society*, 40: 1361-1403.
753 Li XB, Tsai FTC. 2009. Bayesian model averaging for groundwater head prediction
754 and uncertainty analysis using multimodel and multimethod. *Water Resources*
755 *Research*, 45(9): 627-643.
756 Li JY, Liang CH, Du LY. 2014. Effects of Organic Matter on Mercury Adsorption-
757 Desorption in Brown Soil. *Bulletin of Soil and Water Conservation*, 34(6): 32-35, 42.
758 Mendonca T, Melo VF, Alleoni LRF. 2013. Lead adsorption in the clay fraction of two
759 soil profiles from Fildes Peninsula, King George Island. *Antarctic Science*, 25(3): 389-
760 396.
761 Neuman SP. 2003. Maximum likelihood Bayesian averaging of alternative conceptual-
762 mathematical models. *Stochastic Environmental Research & Risk Assessment*, 17(5):
763 291-305.
764 Neuman SP, Xue L, Ye M, and Lu D. 2012. Bayesian analysis of data-worth considering
765 model and parameter uncertainty. *Advances in Water Resources*,36: 75-85.
766 Núñez-Delgado A, Fernández-Sanjurjo MJ, Álvarez-Rodríguez E, Cutillas-Barreiro L,
767 Nóvoa-Muñoz JC, Arias-Estévez M. 2015. Cr(VI) Sorption/Desorption on Pine
768 Sawdust and Oak Wood Ash International. *Journal of Environmental Research and*
769 *Public Health*, 12: 8849-8860.
770 Rose CW, Hogarth WL, Sander GC, Lisle IG, Hairsine PB, Parlange J-Y. 1994.
771 Modeling processes of soil erosion by water. *Trends Hydrol*, 1: 443-451.
772 Razavi S and Gupta HV. 2015. What do we mean by sensitivity analysis? The need for
773 comprehensive characterization of ‘‘global’’ sensitivity in Earth and Environmental

systems models, *Water Resources Research*, 51, doi:10.1002/2014WR016527.

Riva M, Guadagnini A, Dell'Oca A. 2015. Probabilistic assessment of seawater intrusion under multiple sources of uncertainty, *Advances in Water Resources*, 75: 93-104.

Ranaee E, Riva M, Porta GM, Guadagnini A. 2016. Comparative assessment of three-phase oil relative permeability models. *Water Resources Research*, 52(7).

Schwarz G. 1978. Estimating the dimension of a model. *The Annals of Statistics*, 6(2): 461-46.

Sharpley AN. 1980. The enrichment of soil phosphorus in runoff sediments. *Journal of Environmental Quality*, 9: 521-526.

Saltelli A, Ratto M, Andres T, Campolongo F, Cariboni J, Gatelli D, Saisana M, and Tarantola S. 2008. Global Sensitivity Analysis: The Primer, John Wiley & Sons.

Saltelli A, Annoni P, Azzini I, Campolongo F, Ratto M and Tarantola S. 2010. Variance based sensitivity analysis of model output. design and estimator for the total sensitivity index. comput phys commun. *Computer Physics Communications*, 181(2): 259-270.

Sangiumsak N, Punrattanasin P. 2014. Adsorption Behavior of Heavy Metals on Various Soils. *Polish Journal of Environmental Studies*, 23(3): 853-865.

Šimůnek J, Šejna M, Saito H, et al. 2009. The HYDRUS-1D Software Package for Simulating the One-Dimensional Movement of Water, Heat, and Multiple Solutes in Variably-Saturated Media. Version 4.08.

Tong JX, Yang JZ, Hu BX, Bao RC. 2010. Experimental study and mathematical

796 modeling of soluble chemical transfer from unsaturated-saturated soil to surface
797 runoff. *Hydrologic Processes* 24: 3065-3073.
798 Temkin MJ, Pyzhev V. 1940. “Kinetics of Ammonia Synthesis on Promoted Iron
799 Catalysts,” Acta Physiochimica URSS, 12(1): 217-222.
800 Tsai FTC, Li X. 2008. Inverse groundwater modeling for hydraulic conductivity
801 estimation using Bayesian model averaging and variance window. *Water Resources*
802 *Research*, 44(9): 2802.
803 Wallach R, van Genuchten MT. 1990. A physically based model for predicting solute
804 transfer from soil solution to rainfall induced runoff water. *Water Resource Research*,
805 26(9): 2119-2126.
806 Walker J, Walter MT, Parlange J-Y, Rose CW, Meerveld HJT, Gao B, Cohen AM. 2007.
807 Infiltration reduces raindrop-impact driven soil erosion. *Journal of Hydrology*, 342(3-
808 4): 331-335.
809 Winter CL, Nychka D. 2010. Forecasting skill of model averages. *Stochastic*
810 *Environmental Research and Risk Assessment*, 24(5): 633-638.
811 Ye M, Meyer PD, and Neuman SP. 2008. On model selection criteria in multi model
812 analysis. *Water Resources Research*, 44(3): 380-384.
813 Zhang XC, Norton D, Nearing MA. 1997. Chemical transfer from soil solution to
814 surface runoff. *Water Resources Research*, 33(4): 809-815.
815 Zhang XC, Norton D, Lei T, Nearing MA. 1999. Coupling mixing zone concept with
816 convection-diffusion equation to predict chemical transfer to surface runoff. *American*
817 *Society of Agriculture Engineers*, 42(4): 987-994.

818 Zheng CM, and Wang PP. 1998. MT3DMS, A modular three-dimensional multispecies
819 transport model for simulation of advection, dispersion and chemical reactions of
820 contaminants in groundwater systems: Vicksburg, Miss., Waterways Experiment
821 Station, U.S. Army Corps of Engineers.
822

Tables

Table 1. Main chemical characteristics of soil sample 2 used in the experiments.

Cr(VI)	Fe_2O_3	Al_2O_3	MnO	Eh	pH
≤0.015 (mg kg^{-1})	0.0377 (g kg^{-1})	0.0094 (g kg^{-1})	0.0051 (g kg^{-1})	497.31 (mV)	7.6

Table 2. Key parameters and quantities characterizing the experimental conditions.

Experiment	Rainfall intensity, p /(cm min^{-1})	Stable infiltration rate, i_s /(cm min^{-1})	The time start to produce ponding water, t_p /(min)	The time runoff occur, t_r /(min)	The time of infiltration rate reached stable, t_s /(min)
1	0.092	0.028	6.5	27	40
2	0.100	0.024	5.75	28.7	39

Table 3. Maximum Likelihood model parameter estimates and associated standard deviation (SD).

model		L					F				
parameter		α	γ	K_{eq}	S_{max}	h_{mix}	α	γ	K_f	n	h_{mix}
Experiment 1	estimate	0.28	0.78	0.02	69.00	0.37	0.40	0.69	6.61	1.31	0.13
	SD	34.34	12.89	0.44	2753.87	5.61	162.21	96.57	1162.71	5.19	2.84
Experiment 2	estimate	0.15	0.21	0.51	111.00	0.46	0.22	1.0	17.50	2.89	0.88
	SD	10.87	2.16	12.81	1722.21	11.74	76.13	18.52	590.91	50.92	28.85

model		T					H			
parameter		α	γ	K	f	h_{mix}	α	γ	K_d	h_{mix}
Experiment 1	estimate	0.19	0.70	1.13	291.64	0.35	0.13	0.66	0.45	0.38
	SD	3749	988.1	295223.64	1542530.39	1863.25	359.57	69.39	424.10	1.81
Experiment 2	estimate	0.28	0.92	0.004	124.41	0.67	0.035	0.52	0.82	0.70
	SD	98.29	31.00	4.30	13784.77	73.28	390.06	25.67	843.01	5.57

Table 4. Correlation coefficients between model parameters

L model

	α	γ	K_{eq}	$S_{\max}$	h_{mix}
α	**1**	**0.99**	**0.61**	**0.77**	**0.65**
γ	**0.99**	**1**	**0.62**	**0.76**	**0.64**
K_{eq}	**-0.99**	**-0.99**	**1**	**-0.02**	**-0.19**
$S_{\max}$	**0.98**	**0.98**	**-0.97**	**1**	**0.98**
h_{mix}	**0.99**	**0.99**	**-0.99**	**0.99**	**1**

F model

	α	γ	K	n	h_{mix}
α	**1**	**1**	**0.99**	**-0.99**	**0.98**
γ	**0.99**	**1**	**0.99**	**-0.99**	**0.97**
K	**-0.99**	**-0.98**	**1**	**-0.99**	**0.97**
n	**-0.95**	**-0.97**	**0.95**	**1**	**-0.95**
h_{mix}	**0.97**	**0.95**	**-0.97**	**-0.87**	**1**

T model

	α	γ	K_t	f	h_{mix}
α	**1**	**1**	**0.99**	**1**	**1**
γ	**0.99**	**1**	**0.99**	**1**	**1**
K_t	**0.91**	**0.94**	**1**	**1**	**1**
f	**0.98**	**0.99**	**0.96**	**1**	**1**
h_{mix}	**0.99**	**0.99**	**0.95**	**0.99**	**1**

H model

	α	γ	K_d	h_{mix}
α	**1**	**1**	**1**	**-0.97**
γ	**0.99**	**1**	**1**	**-0.97**
K_d	**0.99**	**1**	**1**	**-0.97**
h_{mix}	**-0.43**	**-0.44**	**-0.44**	**1**

Note: the upper and lower triangular regions respectively represent correlation coefficients for experiment 1 and 2.

15 Table 5. Results of model identification criteria for both experiments.

Model	L				F			
Index	AIC	AICC	BIC	KIC	AIC	AICC	BIC	KIC
Experiment 1	-139.29	-134.34	-132.22	-156.22	-139.94	-135.00	-132.87	-155.78
Experiment 2	-36.04	-30.79	-29.23	-56.05	-30.38	-25.13	-23.57	-58.85

Model	T				H			
Index	AIC	AICC	BIC	KIC	AIC	AICC	BIC	KIC
Experiment 1	-80.22	-75.27	-73.15	-135.52	-140.79	-137.46	-134.90	-150.26
Experiment 2	-29.92	-24.67	-23.10	-61.81	-21.71	-18.18	-16.03	-38.45

16

17

18 Table 6. Posterior model weights (%) for the set of alterative models tested.

Model	L				F			
Index	AIC	AIC_C	BIC	KIC	AIC	AIC_C	BIC	KIC
PMW 1	22.18	14.03	16.10	53.97	30.7	19.43	22.30	43.29
PMW 2	90.39	90.30	90.34	4.37	5.32	5.32	5.32	17.76

Model	T				H			
Index	AIC	AIC_C	BIC	KIC	AIC	AIC_C	BIC	KIC
PMW 1	0.00	0.00	0.00	0.00	47.09	66.54	61.60	2.74
PMW 2	4.22	4.22	4.22	77.87	0.07	0.16	0.12	0.00

19 **Note: PMW 1 (or 2) denotes posterior model weights for experiment 1 (or 2)**

Figures

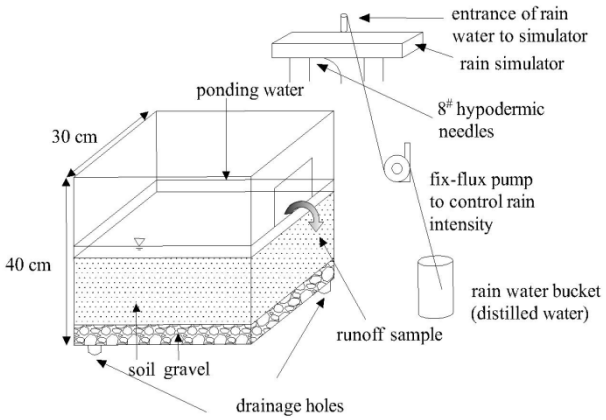

Figure 1. Sketch of the experimental set-up

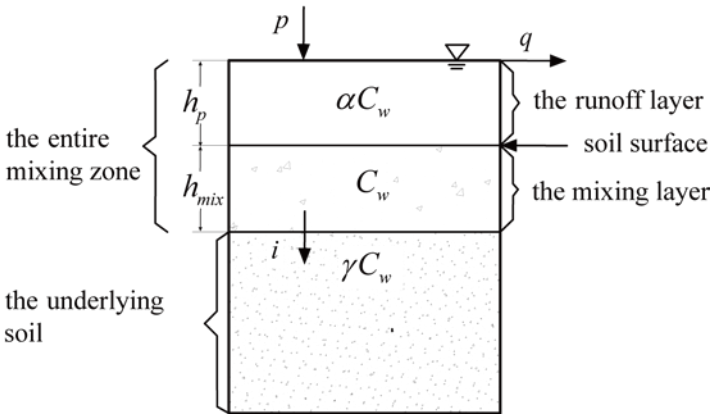

Figure 2. Conceptual depiction of the two-layer model. Notations are: the rainfall intensity p; the specfic discharege rate of overland flow q; the depth of the ponding layer h_p; the depth of the mixing layer h_{mix}; infiltration rate i; the solute concentration in the mixing layer C_w; the solute concentration in the ponding layer /the runoff layer αC_w; the solute concentration in the underlying soil γC_w.

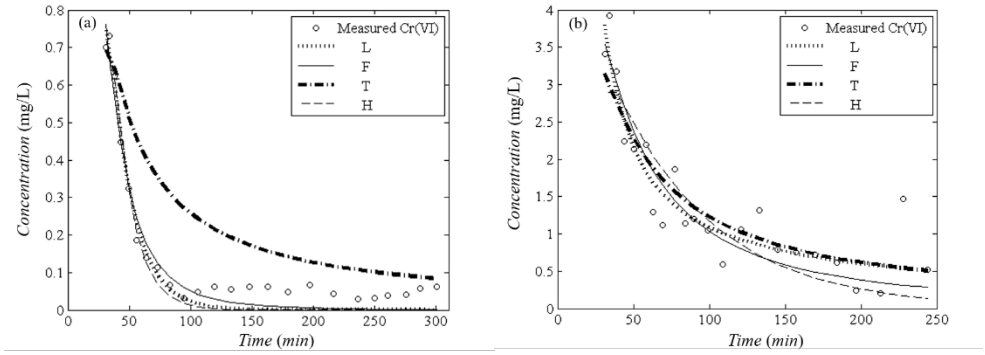

Figure 3. Temporal variation of measured Cr(VI) concentrations in the runoff together with their simulated counterparts based on optimized parameters (L, F, T and H models) for experiments (a) 1 and (b) 2.

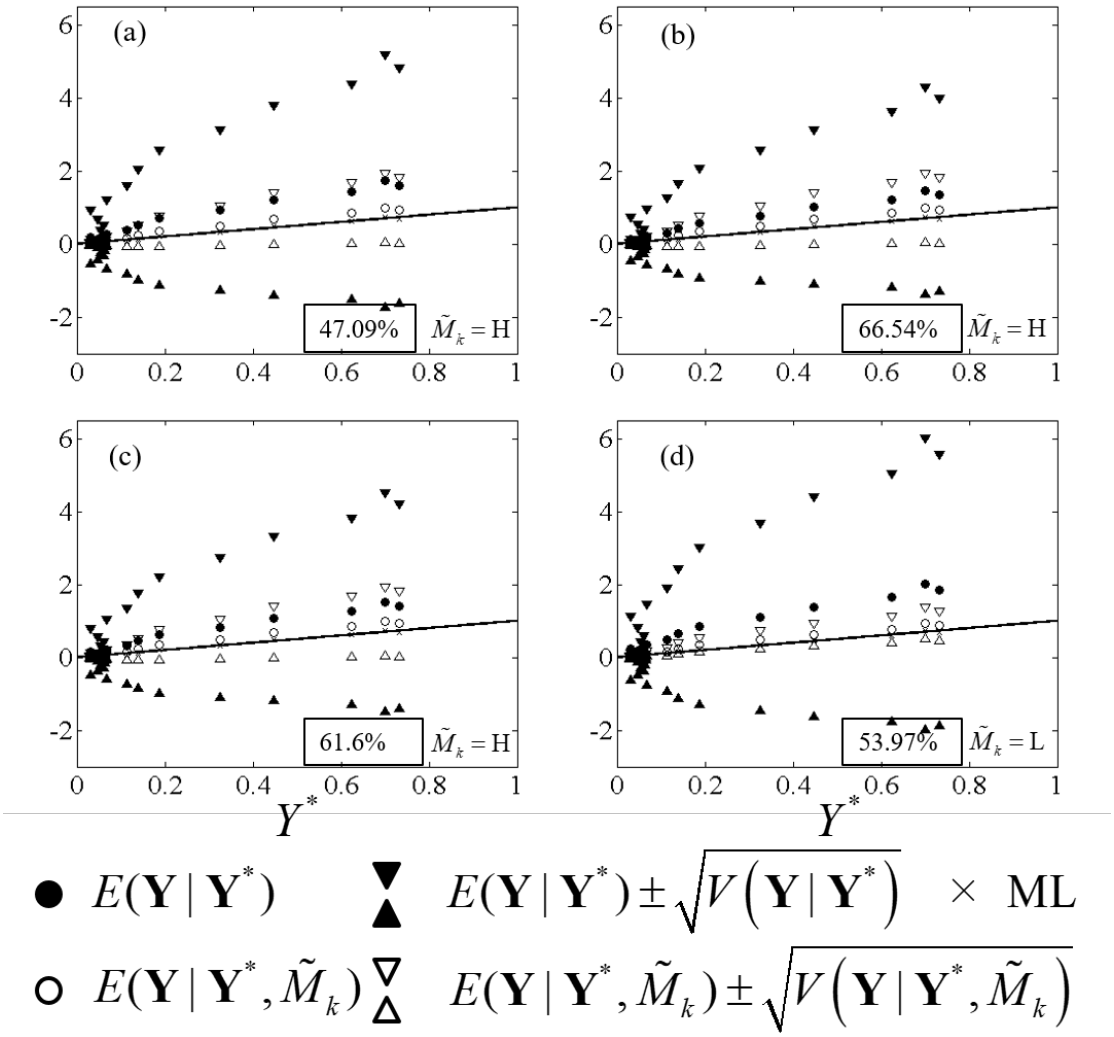

Figure 4. Scatterplots of estimates of Cr(VI) concentration in the surface runoff (collected in vector **Y**) versus data (collected in vector $\mathbf{Y}^*$) of experiment 1. When

used, posterior model weights are evaluated through model identification criterion (a) AIC, (b) AIC_C, (c) BIC, and (d) KIC; $\tilde{M}_k$ represents the most skillful model, as identified by the corresponding criterion.

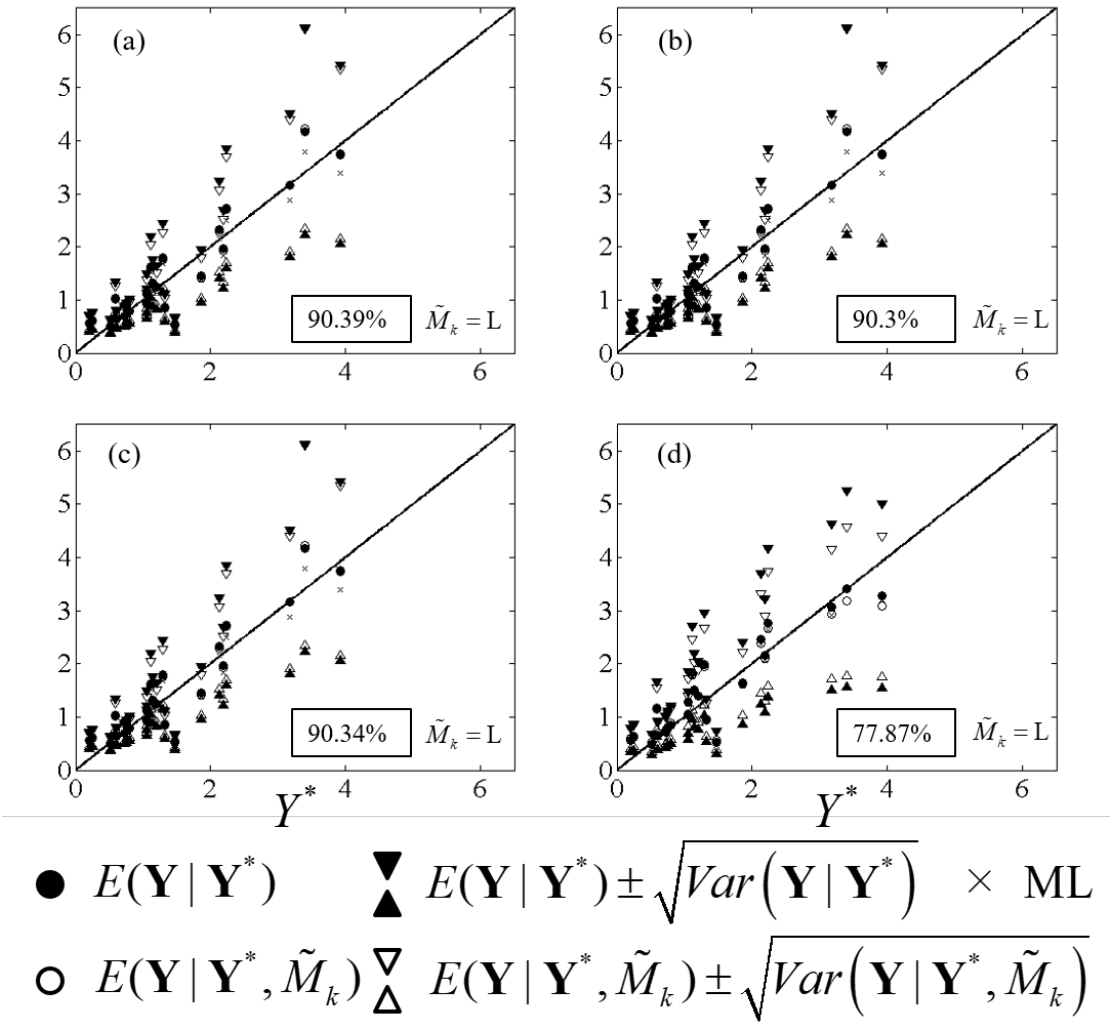

Figure 5. Scatterplots of estimates of Cr(VI) concentration in the surface runoff (collected in vector **Y**) versus data (collected in vector $\mathbf{Y}^*$) of experiment 2. When used, posterior model weights are evaluated through model identification criterion (a) AIC, (b) AIC_C, (c) BIC, and (d) KIC; $\tilde{M}_k$ represents the most skillful model, as identified by the corresponding criterion.

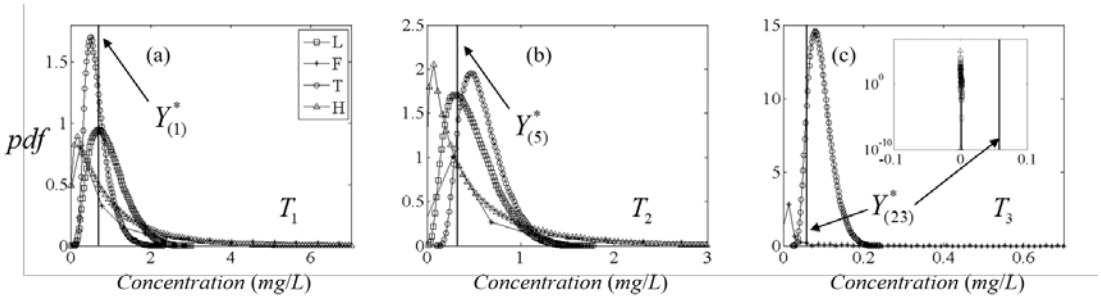

Figure 6. Sample probability density functions (*pdfs*) of Cr(IV) in runoff water (Y) based on the Monte Carlo simulations performed for each model at (a) early (T_1), (b) median (T_2), and (c) late (T_3) simulation times, respectively corresponding to sampling times where observations $Y^*_{(i)}$ (i = 1, 5, and 23), are collected in experiment 1. Vertical lines correspond to measured values $Y^*_{(i)}$.

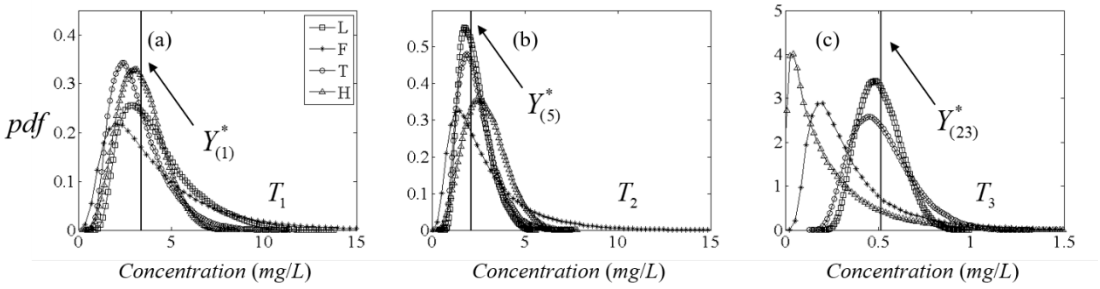

Figure 7. Sample probability density functions (*pdfs*) of Cr(IV) in runoff water (Y) based on the Monte Carlo simulations performed for each model at (a) early (T_1), (b) median (T_2), and (c) late (T_3) simulation times, respectively corresponding to sampling times where observations $Y^*_{(i)}$ (i = 1, 5, and 23), are collected in experiment 2. Vertical lines correspond to measured values $Y^*_{(i)}$.

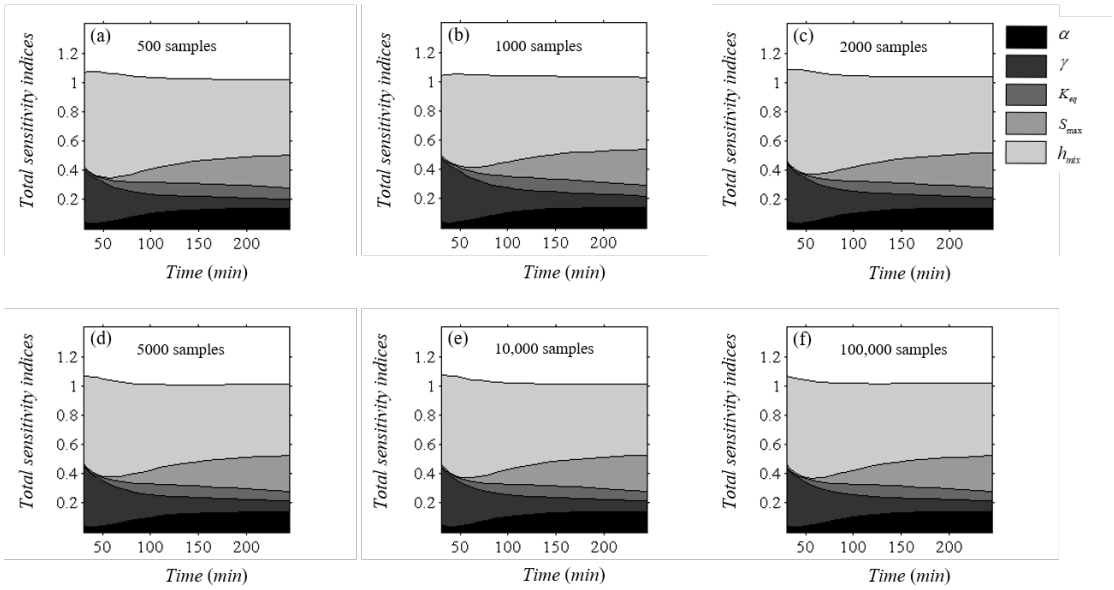

Figure 8. Total sensitivity indices of L model versus time and for diverse sample size, i.e., N = (a) 500, (b) 1000, (c) 2000, (d) 5000, (e) 10,000, and (f) 100,000.

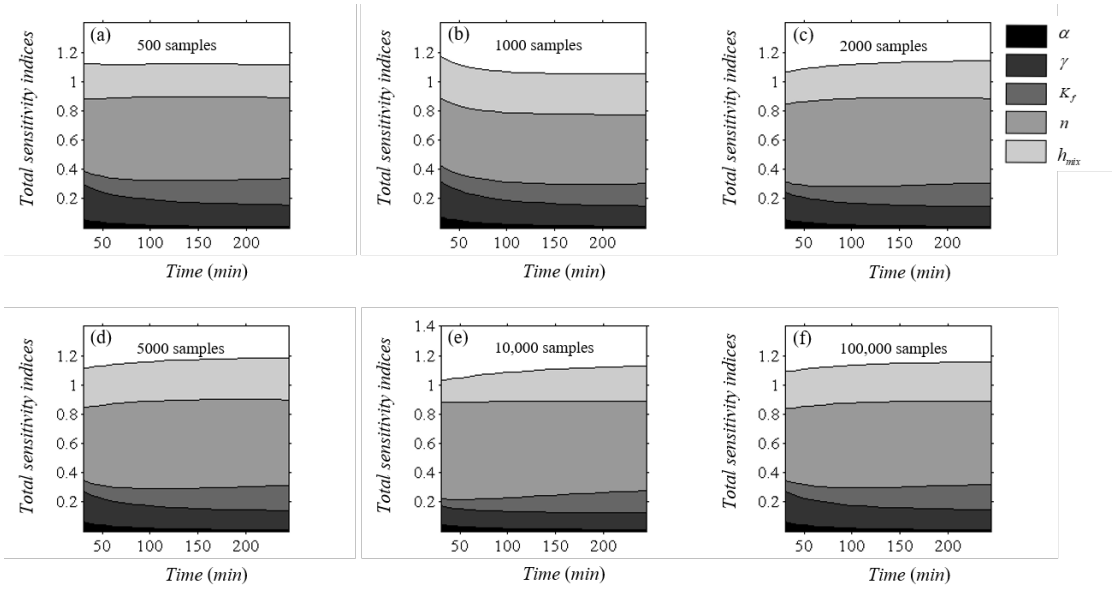

Figure 9. Total sensitivity indices of F model versus time and for diverse sample size, i.e., N = (a) 500, (b) 1000, (c) 2000, (d) 5000, (e) 10,000, and (f) 100,000.

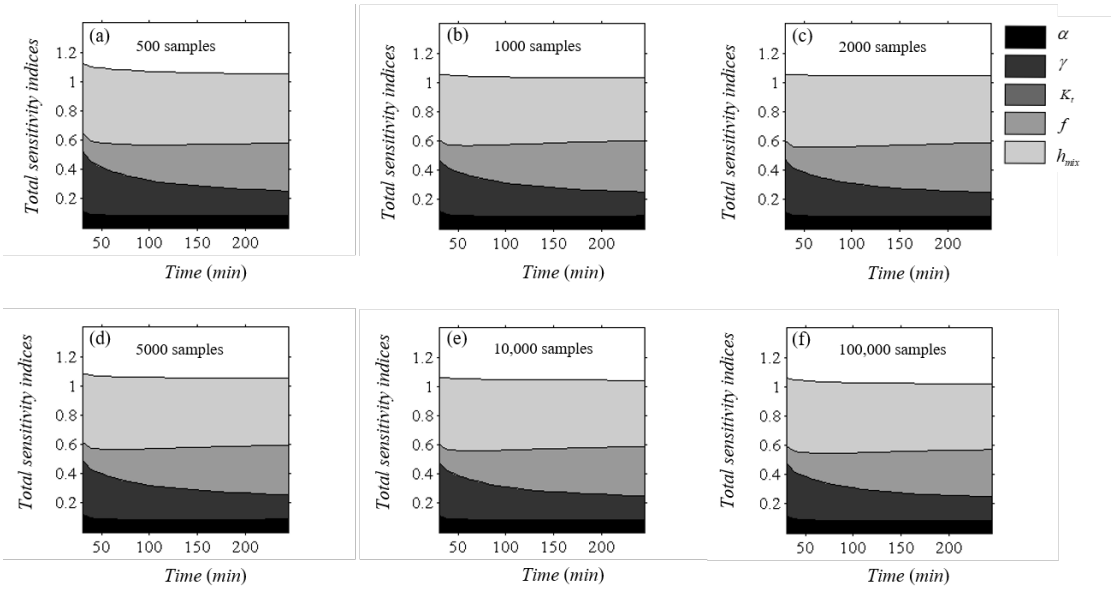

Figure 10. Total sensitivity indices of T model versus time and for diverse sample size, i.e., N = (a) 500, (b) 1000, (c) 2000, (d) 5000, (e) 10,000, and (f) 100,000.

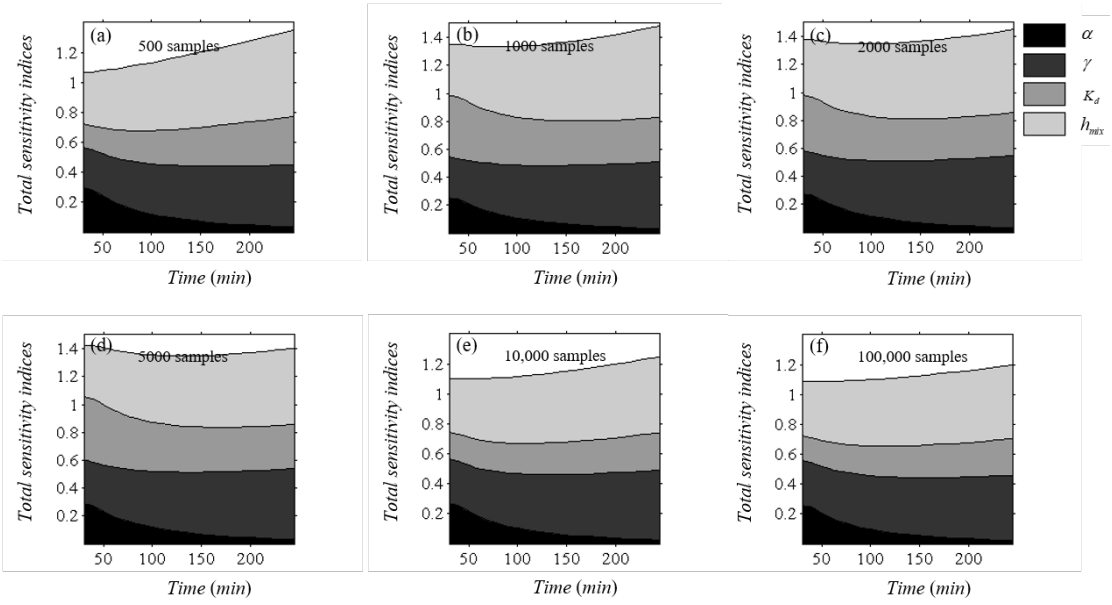

Figure 11. Total sensitivity indices of H model versus time and for diverse sample size, i.e., N = (a) 500, (b) 1000, (c) 2000, (d) 5000, (e) 10,000, and (f) 100,000.

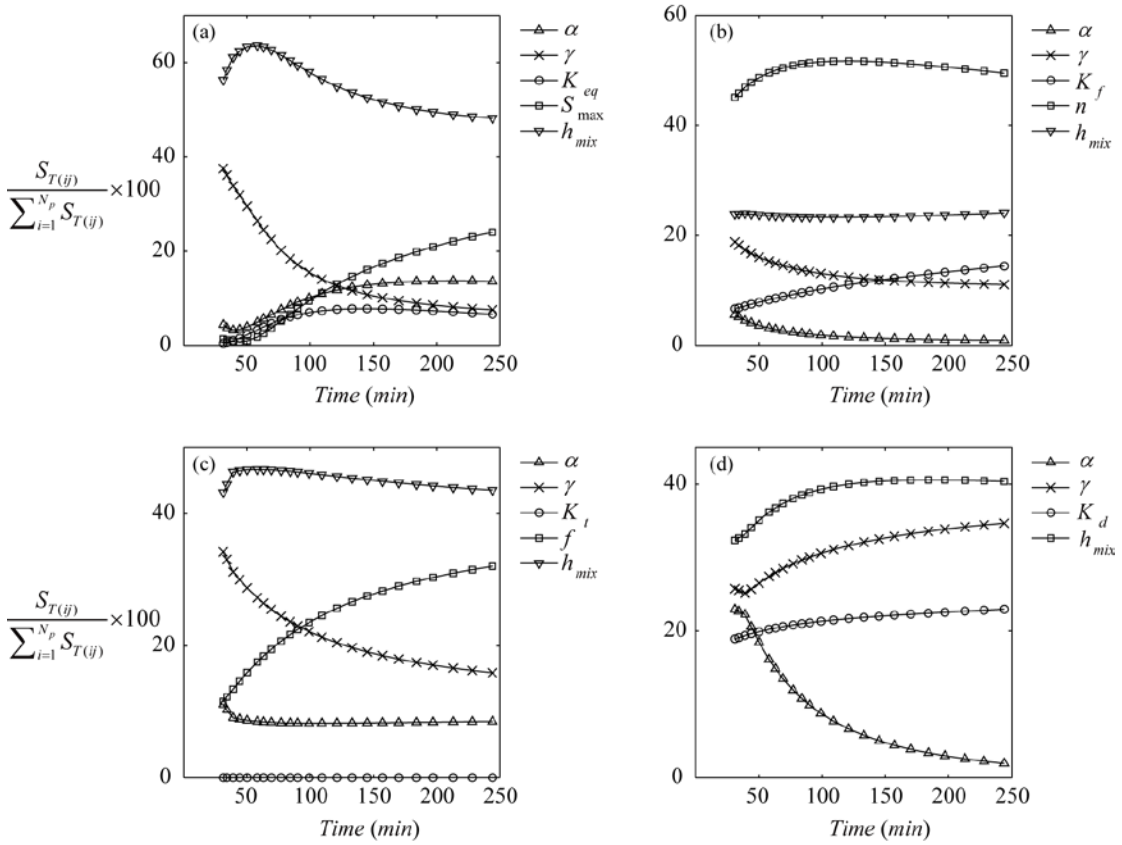

Figure 12. Contributions of each input factor to variation of Cr(VI) in surface runoff versus time for experiment 2 according to model (a) L, (b) F, (c) T, and (d) H.

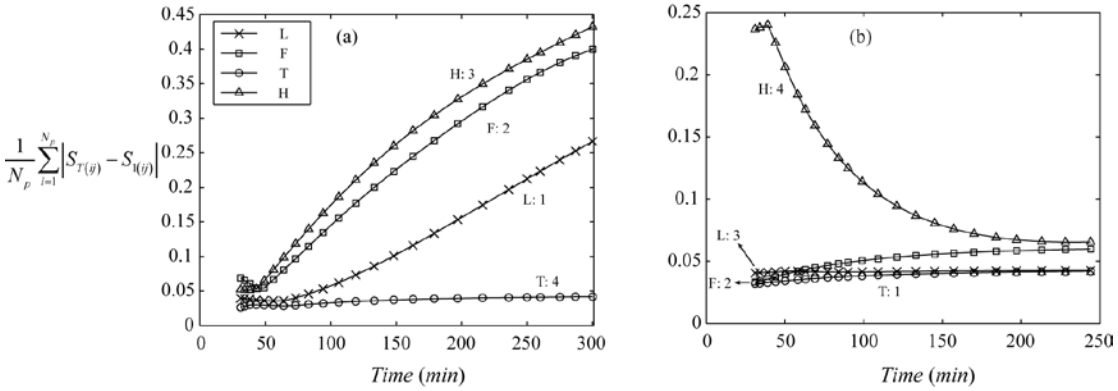

Figure 13. Temporal variation of the mean of the absolute difference between the total ($S_{T(ij)}$) and first-order ($S_{1(ij)}$) sensitivity indices for experiment (a) 1 and (b) 2; the order of model ranking according to the KIC-based posterior model weights are indicated.

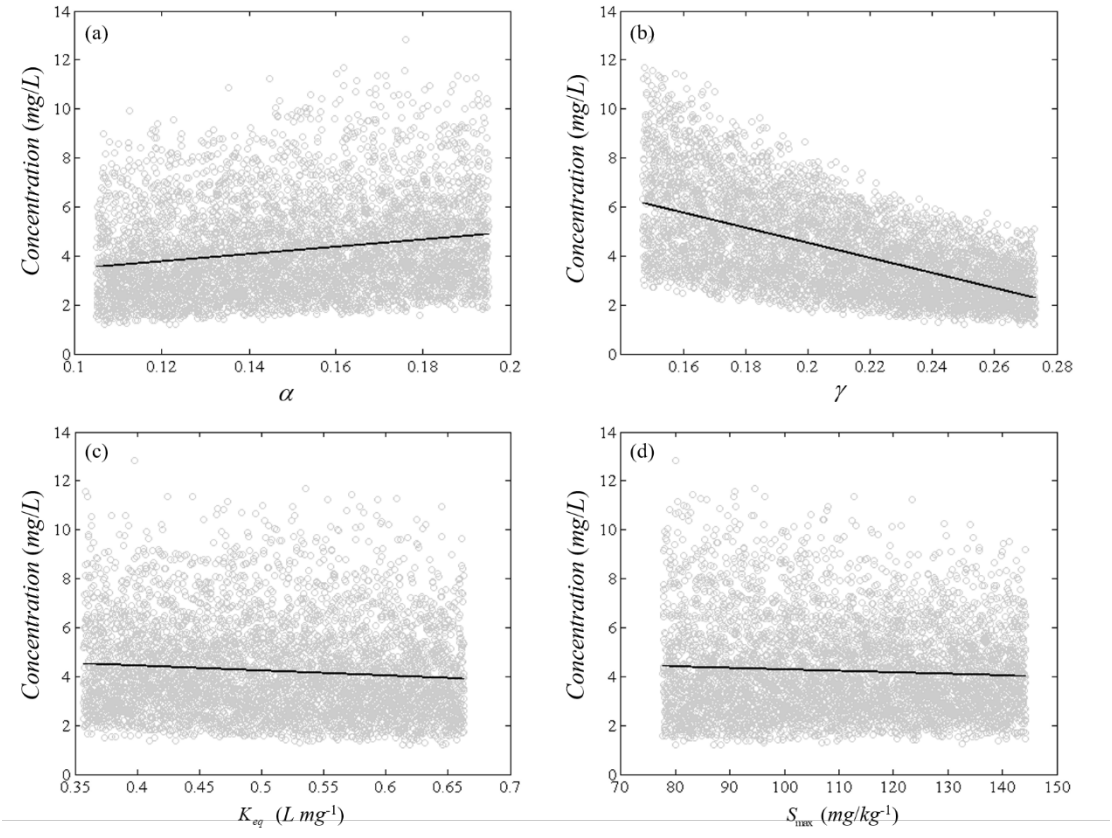

71

72

73 Figure 14. Scatterplots depicting the dependence of model output *Y* and parameters (a)
74 α, (b) γ, (c) K_{eq}, (d) $S_{\max}$, and (e) h_{mix} of the Langmuir coupled tow-layer (L)
75 for experiment 2 at observation time corresponding to the first sampling time. Linear
76 regression curves (solid lines) are included.

77

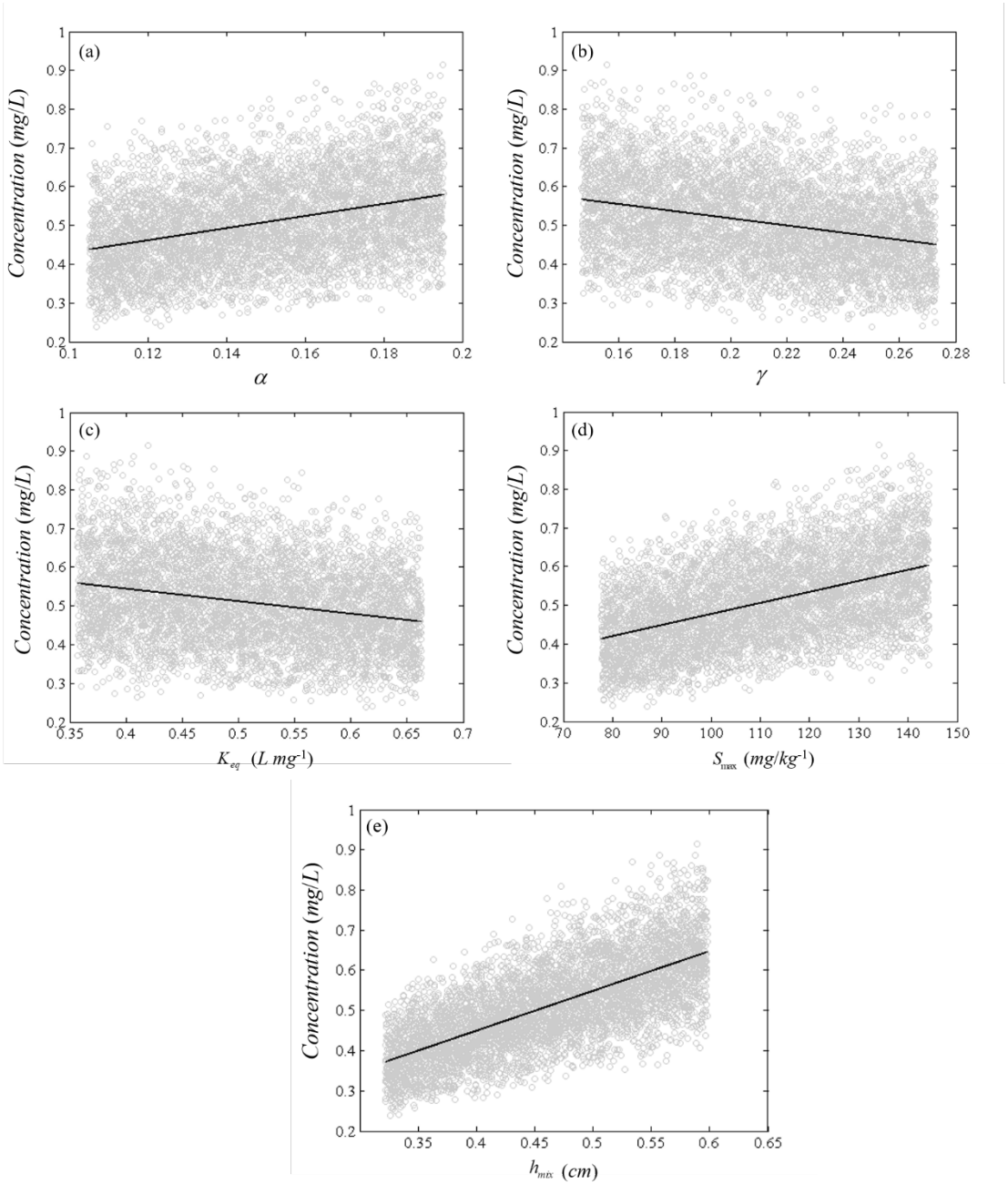

Figure 15. Scatterplots depicting the dependence of model output *Y* and parameters (a) α, (b) γ, (c) K_{eq}, (d) S_{max}, and (e) h_{mix} of the Langmuir coupled tow-layer (L) for experiment 2 at observation time corresponding to the last sampling time. Linear regression curves (solid lines) are included.